JOURNAL OF GEOPHYSICAL RESEARCH, VOL. 115, E07014, doi:10.1029/2009JE003529, 2010

Click Here for Full Article

Four Martian years of nightside upper thermospheric mass densities derived from electron reflectometry: Method extension and comparison with GCM simulations

Robert J. Lillis,[1] Stephen W. Bougher,[2] Francisco González-Galindo,[3] François Forget,[3] Michael D. Smith,[4] and Phillip C. Chamberlin[4]

Received 19 October 2009; revised 22 January 2010; accepted 12 March 2010; published 31 July 2010.

[1] The long-term dynamics of the Martian upper thermosphere near the exobase (~160–200 km) are still relatively poorly constrained by data. Electron reflectometry (ER) provides a way to derive, from electron loss cones, neutral mass densities at these altitudes in the night hemisphere. Because the Mars Global Surveyor Electron Reflectometer was not designed for this purpose, uncertainties in individual measurements are large and thus upper thermospheric variability can be characterized only on time scales of weeks or longer. Density measurements are presented at 2 A.M. local time and 185 km altitude, from April 1999 until November 2006, spanning ~4 Martian years. We observe a weaker correlation with lower atmospheric dust activity than is seen in the lower thermosphere and a weaker correlation with solar EUV flux than is observed in the dayside exosphere. Seasonally repeating features are (1) overall expansion/contraction of the nighttime thermosphere with heliocentric distance, (2) much lower densities at the aphelion winter pole compared to the perihelion winter pole, and (3) a short-lived local density maximum at aphelion in the southern hemisphere. Interannual differences are also observed; in particular, the interval of low densities in the southern winter occurs progressively later as solar EUV flux decreases from solar maximum to solar minimum. Results are compared with predictions from the Mars Thermosphere General Circulation Model and LMD Mars Global Circulation atmospheric model frameworks for Ls = 90°–180°, which generally underestimate and overestimate neutral densities, respectively. This disagreement reflects the difficulty in simulating nightside dynamical and cooling processes.

Citation: Lillis, R. J., S. W. Bougher, F. González-Galindo, F. Forget, M. D. Smith, and P. C. Chamberlin (2010), Four Martian years of nightside upper thermospheric mass densities derived from electron reflectometry: Method extension and comparison with GCM simulations, *J. Geophys. Res.*, *115*, E07014, doi:10.1029/2009JE003529.

1. Introduction

1.1. Martian Thermosphere

[2] The Martian thermosphere is usually referred to as the region of the atmosphere above the mesopause, which is the height at which the atmospheric temperature profile inverts and temperatures begin to increase with altitude. Also around this altitude is the homopause/turbopause, which is the height at which collisions between molecules become sufficiently rare that the individual atmospheric constituents (mainly CO_2, O, CO, N_2, O_2 and Ar) are no longer well mixed and acquire separate scale heights based on diffusive equilibrium. At Mars, they occur at approximately similar attitudes: ~120–130 km on the dayside [*Nier and McElroy*, 1977] and 100–110 km on the nightside [*Forget et al.*, 2009; *McDunn et al.*, 2010]. At its lower boundary, the thermosphere is controlled by the temperatures and densities of the mesosphere, which are influenced by topography [*Withers et al.*, 2003], solar IR heating of the lower atmosphere, and the dynamics of lower atmospheric waves and dust storms [e.g., *Smith*, 2004].

[3] The thermosphere has no commonly accepted upper boundary, overlapping with the lower exosphere at altitudes above the exobase, which was recently given a more general definition by *Valeille et al.* [2009a, 2009b] as the altitude above which a radially escaping particle will encounter one collision on average. Exobase altitudes vary by ~40 km with geographic location, with planet-averaged values ranging from 165 km to 195 km over the Martian year and solar

[1]Space Sciences Laboratory, University of California, Berkeley, California, USA.
[2]Department of Atmospheric, Oceanic and Space Sciences, University of Michigan, Ann Arbor, Michigan, USA.
[3]Laboratoire de Météorologie Dynamique, Institute Pierre Simon Laplace, Paris, France.
[4]NASA Goddard Space Flight Center, Greenbelt, Maryland, USA.

Copyright 2010 by the American Geophysical Union.
0148-0227/10/2009JE003529

Table 1. Mars Thermosphere/Exosphere Investigations

Spacecraft/Instrument	Altitude (km)	Data Product	Month/Year	M-Years	M-Year/L_s	Reference[a]
Viking 1 EDL	0–200 km	T, ρ, species	07/1976	0	12/97°	1
Viking 2 EDL	0–200 km	T, ρ, species	09/1976	0	12/118°	1
Pathfinder ACC	0–160 km	T, ρ	07/1997	0	23/142°	2
MGS ACC 1	110–160 km	T, ρ	09/1997–03/1998	0.31	23/180°–300°	3,4,5
MGS Doppler 1	180 km	ρ	04/1998–09/1998	0.25	23/300°–24/30°	6
MGS ACC 2	110–160 km	T, ρ	09/1998–02/1999	0.20	24/34°–92°	3,4,5
ODY ACC	95–160 km	T, ρ	10/2001–01/2002	0.16	25/258°–314°	4,5
MRO ACC	100–160 km	T, ρ	03/2006–09/2006	0.21	28/35°–99°	7
MGS Doppler 2	390 km	ρ	04/1999–11/2006	3.92	24/150°–28/120°	8
MRO Doppler	250 km	ρ	11/2006–10/2007	0.54	28/135°–330°	9
MGS MAG/ER	180 km	ρ	04/1999–11/2006	3.92	24/150°–28/120°	10, 11
MEX SPICAM	60–130 km	T, ρ	02/2004–04/2006	1.14	26/350°–28/39°	12

[a]References: 1, *Nier and McElroy* [1977] ; 2, *Magalhães et al.* [1999] ; 3, *Keating et al.* [1998]; 4, *Keating et al.* [2003]; 5, *Withers* [2006]; 6, *Tracadas et al.* [2001]; 7, *Tolson et al.* [2008]; 8, *Forbes et al.* [2008]; 9, *Mazarico et al.* [2008]; 10, *Lillis et al.* [2005]; 11, *Lillis et al.* [2008a]; 12, *Forget et al.* [2009].

cycle. As altitude increases beyond the exobase, the thermosphere becomes highly variable [e.g., *Forbes et al.*, 2008; *Mazarico et al.*, 2008] as it interacts directly with the turbulent, shocked solar wind and is increasingly governed by escape processes [e.g., *Lundin et al.*, 2008].

[4] Thermospheric heating is caused by the absorption of solar EUV/UV photons and flow convergence, while cooling is caused by molecular thermal conduction, infrared (IR) radiation and flow divergence [e.g., *Bougher et al.*, 2000, 2009]. The balance between these dynamic and radiative contributions to heating/cooling is a prime determinant of the structure of the Martian thermosphere [e.g., *Bougher et al.*, 2006; *Withers*, 2006; *Bell et al.*, 2007]. While currently unquantified due to a lack of available data, ionospheric currents may also materially impact the thermospheric energy balance and the resulting dynamics [*Withers et al.*, 2005; *Fillingim et al.*, 2010].

1.2. Measurements and Simulations of the Martian Thermosphere

[5] Except for two species-specific atmospheric density profiles provided by the Viking Landers [*Nier and McElroy*, 1977], most published knowledge of the structure and dynamics of the Martian thermosphere comes from (1) accelerometer measurements of atmospheric density, collected during the aerobraking phases of the Mars Global Surveyor (MGS), Mars Odyssey (ODY) and Mars Reconnaissance Orbiter (MRO) missions [e.g., *Keating et al.*, 1998, 2003; *Tolson et al.*, 2008], (2) precise Doppler tracking measurements of the MGS [*Tracadas et al.*, 2001; *Forbes et al.*, 2008] and MRO [*Mazarico et al.*, 2008] spacecraft, (3) mass density measurements inferred from superthermal electron pitch angle distributions (PADs) [*Lillis et al.*, 2005, 2008a] and (4) stellar occultation measurements of temperatures and densities made by the Mars Express (MEX) SPICAM instrument [*Forget et al.*, 2009; *McDunn et al.*, 2010]. SPICAM nightglow (NO*) and dayglow measurements also serve to constrain the Mars thermospheric circulation and variations with Mars' seasons [*Bertaux et al.*, 2005; *Leblanc et al.*, 2006].

[6] From these measurements, significant discoveries have been made about general atmospheric structure [*Keating et al.*, 1998, 2003; *Bougher et al.*, 1999a], zonal density variations caused by thermal tides in the lower thermosphere [*Joshi et al.*, 2000; *Forbes et al.*, 2002; *Wilson*, 2002; *Withers et al.*, 2003; *Bougher et al.*, 2004; *Angelats i Coll et al.*, 2004] and upper thermosphere [*Mazarico et al.*, 2008], solar control of exospheric temperatures [*Forbes et al.*, 2008; *Bougher et al.*, 2009], sub-freezing mesopause temperatures in northern summer [*Forget et al.*, 2009; *McDunn et al.*, 2010], baroclinic instabilities [*Seth and Brahmananda Rao*, 2008], seasonally dependent meridional density gradients [*Withers*, 2006] and global circulation patterns, including strong northern winter polar warming [*Bougher et al.*, 2006].

[7] These discoveries have served as invaluable input for models of global upper atmospheric circulation [*Bougher et al.*, 1990, 1999a, 1999b, 2000, 2004, 2006; *Angelats i Coll et al.*, 2005; *Bell et al.*, 2007; *Forget et al.*, 2009; *González-Galindo et al.*, 2009], which continue to evolve, both as the physical basis for understanding observations and for directing safe and efficient spacecraft aerobraking operations. Despite 11 past spacecraft investigations (summarized in Table 1), the sampling is not nearly complete with respect to season, solar activity, altitude, latitude and local time.

1.3. Prior Probing of Upper Thermospheric Densities With MGS MAG/ER

[8] As presented in papers by *Lillis et al.* [2005, 2008a], we have previously used pitch angle distributions (PADs) of magnetically reflecting superthermal electrons measured at the MGS mapping orbit altitude of 370 km–430 km to constrain neutral mass densities on the nightside at the mean altitude (180–185 km) where the precipitating electrons' scattering depth (analogous to optical depth) reaches unity. This technique required accurate knowledge of the strength and geometry of the crustal magnetic field lines to which the electrons are bound. Therefore it was limited to just ~1–2% of the geographic area of Mars where the unchanging crustal field is strong enough to dominate over the highly variable external magnetic field and where the magnetic topology is 'open' (i.e., the crustal field lines connect to the interplanetary magnetic field (IMF), allowing solar wind electrons access to the collisional atmosphere). This region is shown in Figure 6b. Dayside measurements are not possible using this technique because (1) external magnetic fields are stronger and less predictable, (2) magnetic field lines at 400 km on the dayside connect far less frequently with the collisional atmosphere and (3) photoelectrons produced on the dayside contaminate the pitch angle distributions.

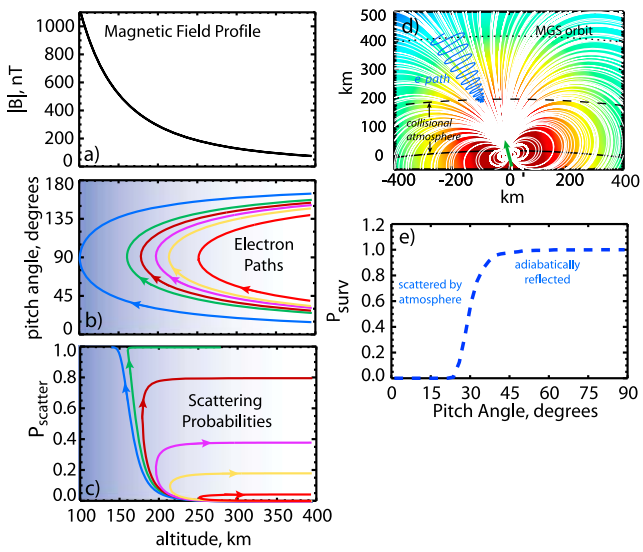

Figure 1. (a) A typical magnetic field-altitude profile for a region of strong crustal field. (b) The pitch angle evolution which this profile dictates for electrons starting at 400 km altitude at 6 different pitch angles: 15, 24, 27, 30, 33, 40 degrees (i.e., the pitch angle at the lower right end of each line) in the absence of any electrostatic potential. (c) The resulting cumulative scattering probabilities for the same electron paths in Figure 1b) for 200 eV electrons as they travel down in altitude and back up again through a typical MTGCM neutral density profile simulated for solar moderate, equinox conditions at the equator at 2 A.M. local time. (d) A two-dimensional illustration showing the magnetic topology of an open crustal magnetic field line region, the helical path of precipitating electrons, MGS mapping orbit altitude (~400 km) and approximate altitude range of the collisional atmosphere. The green arrow represents the direction of crustal magnetization. (e) The resulting adiabatic loss cone, i.e., the survival probability as a function of initial pitch angle. In Figures 1b and 1c arrows show the electrons' direction of motion while the gradient in light blue from right to left approximately represents atmospheric density as a function of altitude and is meant as a visual aid to demonstrate that electrons with initial pitch angles further from 90° encounter higher atmospheric densities and are therefore more likely to scatter. Adapted from *Lillis et al.* [2008b, 2009].

[9] In section 2 we present a necessary summary of the aforementioned technique and proceed to show how an iterative approach can be used to extend this density probing to ~35% of the Martian surface. Section 3 deals with systematic and statistical uncertainties, as well as data coverage. In section 4 we present atmospheric density results and discuss the seasonally repeating and 'anomalous' features therein. In section 5 we compare these results with predictions from two of the leading models of the Mars thermosphere, the National Center for Atmospheric Research (NCAR) Mars Thermosphere General Circulation Model and the Laboratoire de Météorologie Dynamique ground-to-exosphere Global Circulation Model (LMD-MGCM). Section 6 contains conclusions.

[10] The results presented here should help place in context the comprehensive measurements of solar drivers, escape rates and upper atmospheric and ionospheric processes that will be made by the MAVEN Mars Scout mission, which will begin taking data in late 2014.

2. Methodology

2.1. Electron Reflectometry

[11] The theory of electron reflectometry was originally developed for airless bodies by *Anderson et al.* [1976], and extended for use in a planetary atmosphere by *Lillis et al.* [2004, 2008b]. We summarize it below, presenting a model for loss cone formation, the parameters of which may be constrained by least squares fitting to loss cones measured by MAG/ER.

[12] Consider 90–400 eV solar wind electrons traveling along magnetic field lines toward Mars on the nightside (these are the energies for which MAG/ER PADs are most reliable). The electrons' gyroradii are small enough (<~5 km) that they can be considered 'bound' to the magnetic field lines and their magnetic moment (or first adiabatic invariant) is conserved. We define x as distance along the magnetic field line to which the electron is bound, starting at zero at the spacecraft altitude. In this case an electron with initial pitch angle α_0 where the magnetic field is B_0, traveling downward toward Mars along an open field line, will magnetically reflect at point x_r when the field reaches the 'mirror field' $B_m = B_0/\sin^2 \alpha_0$. It will then return, traveling upward, to the initial point with pitch angle $180° - \alpha_0$, while its pitch angle at any point x along its path satisfies the adiabatic condition: $\sin^2\alpha(x) = \sin^2\alpha_0\, B(x)/B_0$ [*Parks*, 2004]. Therefore, downward-traveling electrons on open magnetic field lines in the vicinity of crustal magnetic sources (shown in Figure 1d) with α_0 further from 90° must reach a higher value of B_m before magnetically reflecting and so have a higher probability of scattering in the atmosphere before completing their round-trip back to the spacecraft. The result is a pitch angle-dependent attenuation of the upward-traveling electron flux known as a loss cone (a term we shall use frequently). Loss cones measured by MAG/ER are shown in Figures 3a and 3b.

[13] An electrostatic potential along the field line $\Delta V(x)$ modifies the above picture because it accelerates the electron parallel to the magnetic field line, altering its pitch angle and raising or lowering its reflection altitude. Electrons with lower initial energies are more affected than those with higher energies, so electrostatic potentials make loss cone shapes energy dependent across our modest energy range of 90–400 eV, whereas they are otherwise energy independent. It can be shown [*Lillis et al.*, 2008b] that an electron's probability of surviving (i.e., not scattering during) the round-trip from an initial point at MGS' orbital altitude (~400 km) to its reflection point and back is given by:

$$P_{surv} = \exp[-D],$$

$$D = 2\sum_i \int_0^{x_r} \frac{\sigma_i(U_0 + e\Delta V(x'))n_i(x')dx'}{\sqrt{1 - \dfrac{B(x')\sin^2\alpha_0}{B_0\left(1 + \dfrac{e\Delta V(x')}{U_0}\right)}}} \quad (1)$$

where Σ is the sum over the different atmospheric neutral species, U_0 is the electron's initial energy, e is the electron charge, $n_i(x)$ and σ_i (U) are the neutral number densities and energy-dependent cross-sections for electron-neutral scattering for species i and D is a convenient dimensionless electron scattering depth (analogous to an optical depth) for the round trip. This equation defines the adiabatic loss cone, i.e., the magnetically reflected electron flux, as a function of initial pitch angle α_0, that would be observed if all scattered electrons were absorbed by the atmosphere and could not scatter back up to the MGS orbit altitude. Figure 1 demonstrates the adiabatic loss cone model.

[14] The adiabatic model is fast but treats the Martian atmosphere as a perfect absorber, which is clearly not the case as incident solar wind electrons scatter off neutrals, resulting in a significant backscattered population which must be correctly modeled and subtracted, using a technique based on a comprehensive Monte Carlo treatment of electron transport that is described fully in section 5.3 and Figures 10–12 of *Lillis et al.* [2008b] and need not be repeated here. The relevant result is that, for every measured loss cone the backscattered component can be effectively subtracted before least squares analysis can be applied using the adiabatic model.

[15] The broad idea behind electron reflectometry in a planetary atmosphere is that we assume a priori knowledge of the profiles (along the magnetic field line) of one or two of the three important variables which determine loss cone shape: magnetic field strength, electrostatic potential and neutral density ($B(x)$, $\Delta V(x)$ and $n_i(x)$ respectively), then use the measured loss cones from MAG/ER to solve for parameters describing the profiles of the remaining variables [*Lillis et al.*, 2008b] at the time and location the loss cone is measured.

[16] In this paper, we shall use an iterative technique in order to calculate the most likely magnetic field profile $B(x)$ for each loss cone, then use the loss cone shapes in different energy channels to constrain parameters describing $\Delta V(x)$ and most importantly for our purposes, $n_i(x)$.

2.2. Calculating the "Most Likely" Magnetic Profile for Each Loss Cone

[17] The magnetic field on the Martian nightside has two components: (1) the permanent, unchanging internal field due to magnetization contrasts in the Martian crust and (2) the dynamic, double-lobed external field of the Martian magnetotail which varies substantially with solar wind pressure and the direction of the interplanetary magnetic field (IMF) [*Crider et al.*, 2003; *Ferguson et al.*, 2005].

[18] In order to use measured loss cones to solve for atmospheric neutral densities, we require accurate knowledge of the total (i.e., internal plus external) magnetic field $B(x)$ between the spacecraft (i.e., measurement) location and the collisional atmosphere where the electrons scatter. Since magnetic field is only directly measured at the spacecraft (B_0 in equation (1)), information for the remainder of the profile must come from elsewhere.

[19] In *Lillis et al.* [2008a], to calculate this profile we used the *Cain et al.* [2003] spherical harmonic model of the internal magnetic field of Mars only in regions where (1) the crustal field is strong enough to dominate the external field, (2) the magnetic field topology allowed loss cones to form and (3) the measured magnetic field at the spacecraft matched the *Cain et al.* [2003] model to within 10° in direction and 5% in magnitude.

[20] The details of the fitting procedure used to retrieve thermospheric mass densities can be found in appendix A of this paper and in the work of *Lillis et al.* [2008a]. However, the relevant result from the ~12,000 reliable fits was the mean loss cone-derived mass density at the altitude of maximum sensitivity (185 km) of 6.6 g/km^3 over ~1.2% of the Martian surface in the southern hemisphere (see Figure 6b) over the ~4 Martian year period from 04/1999–11/2006.

[21] The primary intended purpose of the ER instrument on the MGS spacecraft was to detect and measure weak crustal magnetic fields by the technique of electron reflection magnetometry, which uses measured loss cones to constrain crustal magnetic field magnitudes [*Anderson et al.*, 1976; *Acuña et al.*, 1992]. To accomplish this (essentially the reverse of the method explained in appendix A), *Lillis et al.* [2008c] assumed the fixed neutral atmospheric profile to be an MTGCM-simulated, equatorial, spring equinox, 2 A.M. neutral density profile, multiplied by a scale factor of 1.1 at all altitudes such that its mass density would equal 6.6 g/km^3 at 185 km (i.e., the mean derived density from *Lillis et al.* [2008a]). This profile was intended to be a reference atmosphere that is as close to the mean as possible [*Lillis et al.*, 2008c] and, although the profile only represents densities measured in the southern hemisphere, GCM simulations and accelerometer data taken below 160 km suggest that annual mean density profiles should not be significantly different in the Northern hemisphere.

[22] The magnetic field profile was parameterized by a constant term (the external, 'ambient' field, B_a) plus a crustal term that falls off as a power law (with exponent p, assumed to equal 2.5) with distance z from the crust:

$$B(z) = B_a + (B_{sc} - B_a)\left(\frac{z_{sc}}{z}\right)^p \tag{2}$$

where B_{sc} and z_{sc} are the field magnitude at the spacecraft and distance from the crustal source to the spacecraft respectively and where we assumed a straight-line continuation of the field measured at the spacecraft at an angle θ to the local horizontal.

[23] Figure 2 and equation (3) illustrate the relationship between z, x,θ, the magnetization burial depth d and the altitude h (with respect to which densities are defined).

$$z(h,d,\theta) = R_{Mars}\left[\left(1+\frac{h+d}{h+R_{Mars}}\right)\sin\theta - \sqrt{1-\left(1+\frac{h+d}{h+R_{Mars}}\right)^2\cos^2\theta}\right] \tag{3}$$

Since B_{sc}, Z_{sc}, θ are measured directly for every loss cone, any combination of values of B_a, d and p uniquely determines the model magnetic field magnitude at all altitudes.

[24] However, only magnetic field values in the electron absorption layer (170–210 km) can affect the loss cone shape [*Lillis et al.*, 2008b], with the mean altitude of greatest sensitivity occurring at 185 km. This means that there is no unique 'best' combination of B_a, d and p, i.e., they are

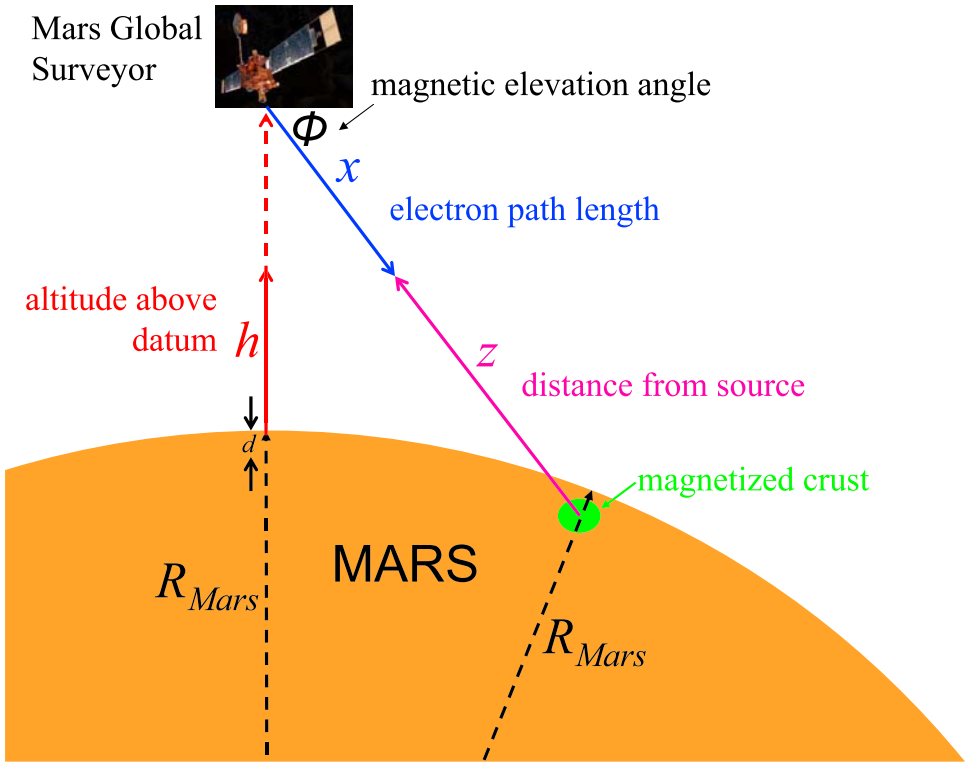

Figure 2. Illustration showing the relationship between altitude h, electron path length x and distance from magnetized source z in terms of the magnetic elevation angle θ, the radius of Mars and the burial depth d of the magnetized material. Equation (3) relates these variables mathematically.

highly correlated (see Figure 12 of *Lillis et al.* [2008c]). Therefore, we chose a fixed value of 20 km for d as approximately half of reasonable estimates of the total mean thickness of Mars' crustal magnetization [*Voorhies*, 2008] and a fixed value of 2.5 for p, which is expected to range between 2 (corresponding to an infinite line of dipoles) and 3 (for a single point dipole). We then solved for the crustal field at 185 km, hereafter referred to as B_{185}, in terms of the dimensionless quantity B_a/B_{sc}, (which conveniently ranges between 0 and 1 for the purpose of fitting). For simplicity and due to the aforementioned low angular resolution of the ER instrument, the electrostatic potential was parameterized in terms of a constant parallel (i.e., to the magnetic field) electric field component which was simultaneously solved for along with B_a/B_{sc}. After discarding poor fits, a data set ~of 1.6 million estimates of B_{185} remained.

[25] At this point, a series of correcting, binning, fitting and smoothing steps were employed to convert the data set of B_{185} values into the magnetic field map shown in Figure 4 of *Lillis et al.* [2008c]. The geophysical applications of this map (e.g., studying impact basins and volcanic structures) demand that it be the most accurate estimate of the crustal-only magnetic field at 185 km altitude, i.e., the field measured *in the absence of any external field*. However, for our current purpose of thermospheric density probing, we are instead interested in the most accurate representation of the total (i.e., crustal + external) magnetic field magnitude between the electron absorption layer and the spacecraft for each particular measured loss cone. This requires examining the interplay between the two components of the magnetic field. The remainder of section 2 is dedicated to the extension of the electron reflectometry technique specific to this application.

[26] Our parameterization of the magnetic profile (equation (2)) necessarily assumes that the variable external and constant crustal components of the vector magnetic field can be added as scalar quantities (i.e., that they are co-linear), which is usually not the case. Therefore the measured loss cone (and hence B_{185}) varies as a function of external field direction, the radial component of which is typically bimodal (i.e., upward or downward) on the Martian nightside as the IMF direction at Mars switches from primarily northward to southward [*Ferguson et al.*, 2005]. This is clearly demonstrated in Figure 16 of *Lillis et al.* [2008b].

[27] Unfortunately, in the presence of any substantial crustal field, we cannot measure the external field direction, only the total field direction, which has a bimodal distribution where B_{185} is weaker than ~35 nT, i.e., where the bimodal external field is generally stronger than the crustal field at spacecraft altitudes of ~400 km (see Figure 19 of *Lillis et al.* [2008c]). Because we have a limited number of reliable B_{185} data points and generally don't sample all directions of external field, the best we can do is divide the values of B_{185} in each pixel into cases where the measured (i.e., total) magnetic field direction is upward or downward, then calculate the modal value of B_{185} separately for the 'up' and 'down' distributions (explained in more detail in appendix F of *Lillis et al.* [2008c].) Recall that these modal values have been calculated using 4 Martian years of B_{185} values for which a single mean model atmosphere was assumed.

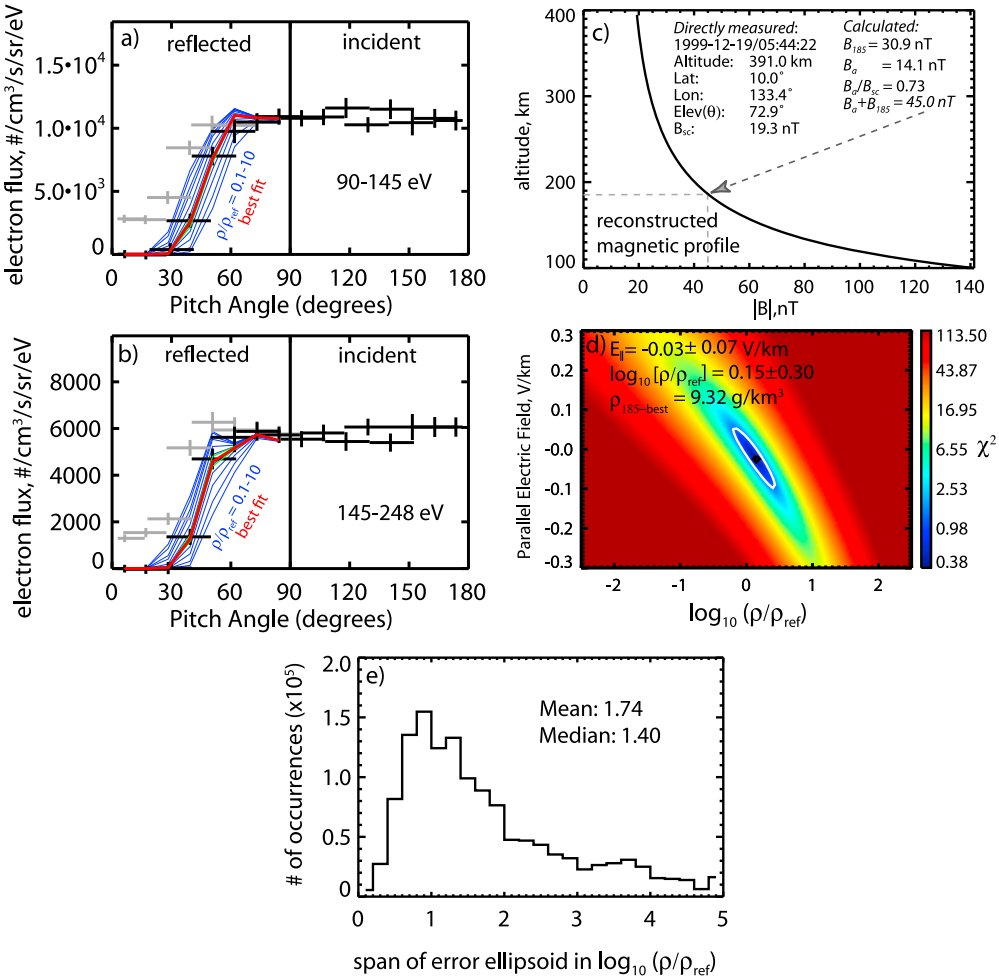

Figure 3. Fit to a typical loss cone. (a and b) Typical electron loss cones measured at 1999-12-19/05:44:22 in two adjacent energy channels. The incident and reflected (i.e., down- and up-traveling) flux are on the right and left, respectively. The flux measurements before backscatter subtraction are shown in gray, while those after are shown in black. The best fit to the loss cone is shown in red, while the predicted loss cone shapes for values of ρ/ρ_{ref} (i.e., the ratio between mass density and a reference density, see text) between 0.1 and 10 are shown in blue. (c) The most likely magnetic field profile used in calculating the predicted loss cones (see text in section 2.2). (d) The χ^2 landscape for this particular fit with the 1-σ error ellipsoid shown in white. ρ_{185} refers to the best estimate of the mass density at 185 km derived from this particular loss cone. (e) The distribution of the span of the error ellipsoid in $\log_{10}\rho/\rho_{\mathrm{ref}}$ over the entire usable data set (i.e., including only data points with magnetic elevation angles greater than 40° and values of B_{185} greater than 15 nT, as discussed in section 3.1).

[28] Hence, for the purpose of constraining thermospheric densities, we trace the measured magnetic field line in three dimensions from the spacecraft position (i.e., latitude, longitude, altitude) in a straight-line down to a new 'remote' latitude and longitude at 185 km altitude. We then use the aforementioned modal value of B_{185} corresponding to the measured field polarity (i.e., up or down), along with the measured quantities B_{sc}, Z_{sc}, θ, to calculate the most likely value of B_a/B_{sc} for the measured loss cone. Using equation (2), we obtain:

$$B_a/B_{sc} = 1 - \frac{B_{185}}{B_{sc}}\left(\frac{z_{185}}{z_{sc}}\right)^p \tag{4}$$

where z_{185} is the value of z at h = 185 km altitude as defined by equation (3). From this value of B_a/B_{sc}, the most likely model magnetic profile $B(z)$ can be calculated:

$$B(z) = B_{sc}\left[1 - B_a/B_{sc}\left(1 - \left(\frac{z_{sc}}{z}\right)^p\right)\right] \tag{5}$$

2.3. Fitting Procedure to Constrain Atmospheric Properties

[29] The next task is to compare the measured, backscatter-subtracted loss cone to predicted loss cones, calculated (using equation (1)) with the magnetic profile from equation (4), but varying the electrostatic potential difference and neutral

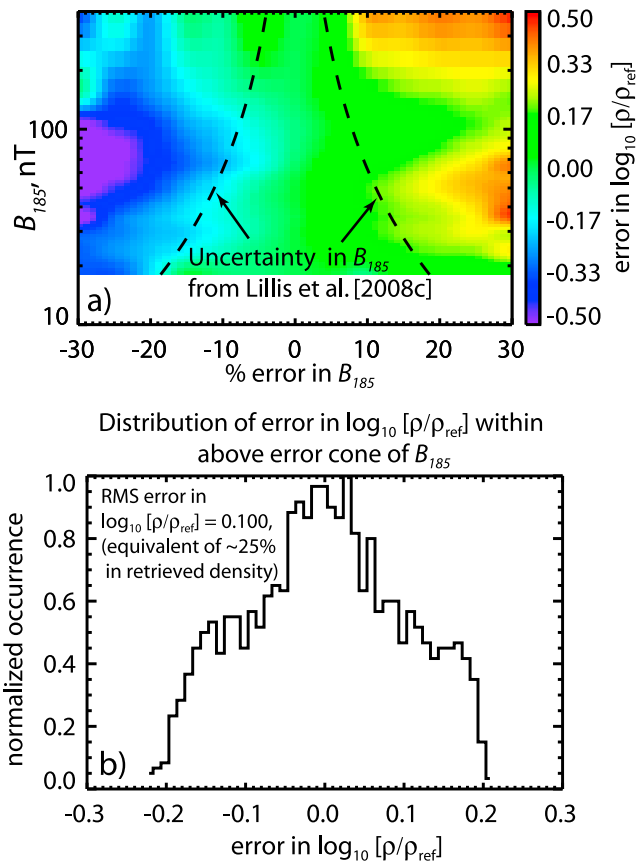

Figure 4. How uncertainties in the assumed value of B_{185} affect uncertainties in ρ/ρ_{ref}. (a) The error in $\log_{10}[\rho/\rho_{ref}]$ as a function of B_{185} and its percentage error (i.e., ΔB_{185}), calculated by artificially increasing/reducing the assumed value of B_{185} for ~12,000 loss cones measured during the interval November 1–15, 1999. The dashed black lines represent ΔB_{185} as a function of B_{185}, as determined by *Lillis et al.* [2008c]. (b) The uncertainties in $\log_{10}[\rho/\rho_{ref}]$ found between the dashed black lines in Figure 4a. The RMS error in $\log_{10}[\rho/\rho_{ref}]$ is 0.100, equivalent to a density uncertainty of 25%.

density profiles until a best fit is achieved. We choose to parameterize each of these profiles with a single parameter in order to make the fitting procedure tractable and because (as mentioned above) the intrinsic angular resolution of the ER instrument does not allow us to constrain additional parameters in any case.

[30] We parameterize the electrostatic profile $\Delta V(x)$ by a single constant electric field component parallel to the magnetic field, $E_{\|}$, over the distance between the spacecraft and the absorption layer. Thus, $\Delta V(x) = eE_{\|}x$ where e is the electron's charge, which is included so the potential has the same units as the electron energy, i.e., electron volts.

[31] We parameterize the neutral density profile $n_i(x)$ with a single scale factor ρ/ρ_{ref} by which we multiply our aforementioned mean model reference atmosphere at all altitudes (see section 2.2). *Lillis et al.* [2008a] showed that the loss cone shapes are sensitive only to the total mass density in the electron absorption layer, so a more complex parameterization is unnecessary.

[32] In order to perform the fitting, we include all 3 of the electron energy channels with sufficient fluxes (90–145 eV, 145–248 eV, 248–400 eV), convolve the modeled loss cones to the overlapping pitch angle bins specific to each individual measured loss cone, and calculate the goodness-of-fit χ^2 for a range of values of $E_{\|}$ and ρ/ρ_{ref}. Figure 3 demonstrates a typical fit, showing the measured loss cones in 2 of the energy channels (Figures 3a and 3b) overlaying the best fit and all predicted loss cones for the optimal value of $E_{\|}$ and values of ρ/ρ_{ref} between 0.1 and 10, the magnetic profile (Figure 3c) and the χ^2 space with the 1-σ error ellipsoid (Figure 3d). For the purposes of this paper, retrieved values of $E_{\|}$ will be treated as a necessary correction only and will not be examined. We shall concentrate only on ρ/ρ_{ref}.

[33] We observe that a single measured loss cone places quite a loose restriction on the neutral mass density in the electron absorption layer; the 1-σ error ellipsoid in Figure 3d spans a factor of ~5 in neutral density, while the median span across the entire data set is 1.4 orders of magnitude, as shown in Figure 3e. Therefore the a priori uncertainty in each density retrieval, derived directly from the uncertainties in the electron flux (as measured by the ER instrument) and propagated through equation (1), is on average 0.7 (i.e., half of 1.4) orders of magnitude, or a factor of 5. Note that this is the statistical uncertainty in a single measurement and does not include systematic uncertainties introduced by the roughly ~20% uncertainties in the electron-neutral scattering cross sections [*Sung and Fox*, 2001] or uncertainties in *B(z)* (i.e., equation (4)) which will be dealt with in the next section.

3. Uncertainties in Retrieved Densities and Data Coverage

3.1. Systematic Uncertainties and Filtering of Unreliable Magnetic Field Profiles

[34] As discussed above, the value of ρ/ρ_{ref} that we retrieve from each loss cone depends upon the value of B_{185} (i.e., crustal-only field at 185 km), which is assumed constant in time at 185 km at the geographic location through which the 'straight' magnetic field line measured at the spacecraft passes. Therefore, systematic errors in ρ/ρ_{ref} should depend both upon errors in B_{185} and upon errors in this tracing.

[35] To investigate the former, we analyzed a 2-week sample of MAG/ER data from November 1–15, 1999 and artificially increased/decreased the assumed values of B_{185} by 13 evenly spaced amounts between −30% and +30%, then plotted the change in the retrieved value of $\log_{10}[\rho/\rho_{ref}]$, as shown in Figure 4a. To a good approximation, *Lillis et al.* [2008c] found that the uncertainty in B_{185} in a given 0.5° × 0.5° geographic bin, ΔB_{185} is given, in units of nT, by:

$$\Delta B_{185} = 0.79\sqrt{B_{185}} \tag{6}$$

[36] The cone of uncertainty defined by equation (6) is shown by dashed black lines in Figure 4a. The uncertainties in $\log_{10}[\rho/\rho_{ref}]$ found within this cone are plotted in Figure 4b and have an RMS error of 0.100, equivalent to a density uncertainty of 25%. In practice, in order to get sufficiently large sample sizes, we will be accumulating ρ/ρ_{ref} over

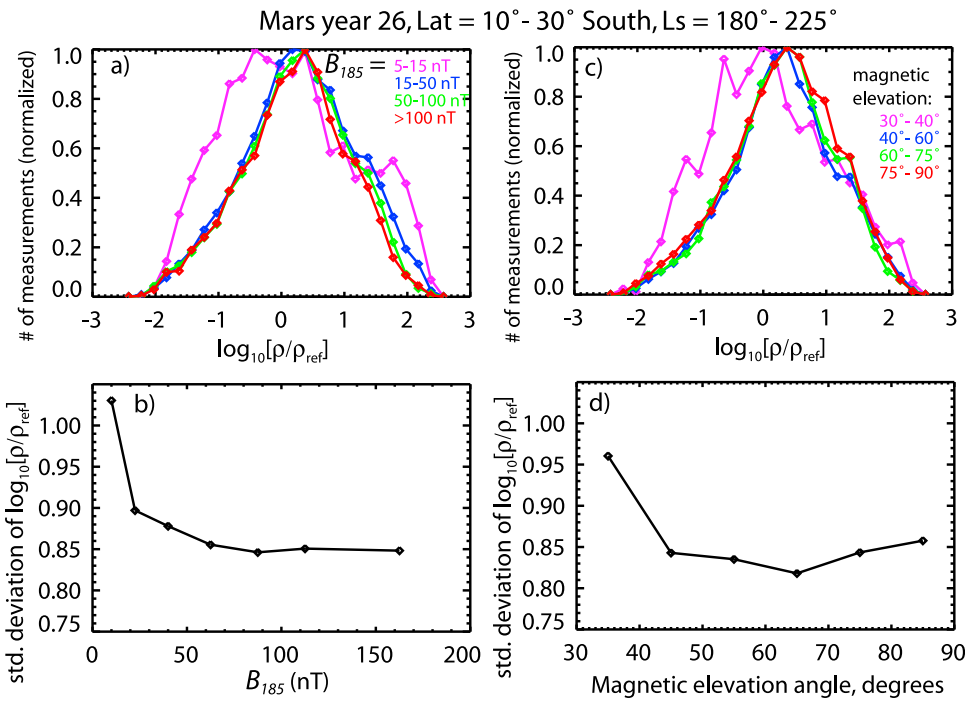

Figure 5. Distributions of ρ/ρ_{ref}, for Mars year 26, Ls = 180°–225°, latitude 10°–30° S, categorized by (a and b) B185 and (c and d) magnetic elevation angle. For the purposes of interpretation, we eliminate all data with B_{185} < 15 nT and elevation angle < 40°.

hundreds of square degrees of the planet for a single time interval, so we expect values of ΔB_{185} to average close to zero. Therefore we don't expect errors in B_{185} to be a substantial contribution to errors in ρ/ρ_{ref}.

[37] Straight field lines from spacecraft altitude (~400 km) to 185 km were assumed in the construction of the map of B_{185} [*Lillis et al.*, 2008c]. Therefore, we do not expect further uncertainties in our assumed magnetic profile from the fact that these field lines may be curved, i.e., as long as crustal fields are strong enough and the distance from the spacecraft to the absorption region is not too large, electrons will see close to the same magnetic profile in the same locations. We expect the most variability in the magnetic profile at a fixed location when the crustal field is weak or the magnetic elevation angle (θ in Figure 2 and equation (3)) is low (i.e., indicating a larger spacecraft-to-absorption region distance) and this is what we observe. Figure 5 plots the distributions of $\log_{10}[\rho/\rho_{ref}]$ for a single span of latitude and Ls, separately for different ranges of B_{185} and magnetic elevation angle. We observe that the character of the distributions are very similar for B_{185} > 15 nT and elevation angle > 40°, but quite different and wider for B_{185} < 15 nT and elevation angle < 40°. Therefore, we shall eliminate all retrieved values of ρ/ρ_{ref} from loss cones in these latter ranges. Indeed, *Lillis et al.* [2008c] ignored loss cones with elevation angles of less than 40° when constructing the map of B_{185} because of the location uncertainty of the field line at 185 km. In our case, the straight field-line assumption does lead to an error in the geographic location of the measurement, but this will be less than 150 km, or 2.5° of latitude, in the vast majority of cases (see appendix D of *Lillis et al.* [2008c]) and is therefore not of concern when discussing global upper thermosphere density trends.

[38] We also investigated the dependence of ρ/ρ_{ref} on the solar wind pressure proxy of *Crider et al.* [2003] and found no statistically significant correlation, implying that the combined effects of solar wind pressure on densities at 185 km and compression of the crustal fields on the night side are either small or largely cancel each other out.

3.2. Geographic Distribution of Reliable Data

[39] As discussed in section 3.1, reliable measurements of ρ/ρ_{ref} can only be made where the magnetic field topology is open and where the profile of magnetic field magnitude along the field line is stable and predictable (B_{185} > 15 nT and elevation angle > 40°). We shall further restrict the reliable subset of the data to solar zenith angles greater than 113° (where all altitudes up to ~300 km are in darkness), in order to avoid sunlight-produced photoelectrons traveling up the magnetic field lines and 'contaminating' the loss cones, which are assumed to consist entirely of magnetically reflected and backscattered solar wind electrons.

[40] These restrictions leave 673,487 valid measurements of ρ/ρ_{ref} from April 1999 until November 2006, located in a geographical pattern determined by the aforementioned restrictions. This data coverage pattern is shown in Figure 6 and compared with the extremely limited data coverage from *Lillis et al.* [2008a]. In terms of the area-normalized percentage of 5° × 5° bins containing at least 100 data points, the work of *Lillis et al.* [2008a] covered 1.2% of the planet's area compared with 36.4% for the present study, a substantial increase.

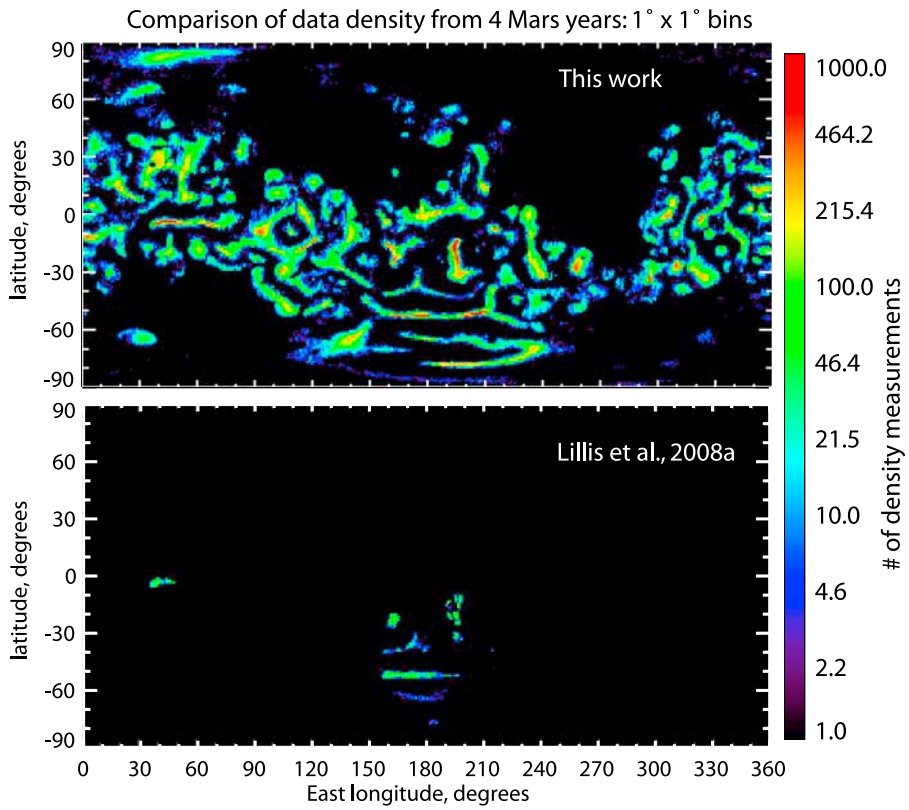

Figure 6. Comparison of geographic data coverage in 1° × 1° bins between this work and that of *Lillis et al.* [2008a]. The total numbers of data points are ~673,000 versus ~12,000 and the total area-normalized percentage of 5° × 5° regions containing at least 100 data points is 36.4% versus 1.2%, respectively.

3.3. A Posteriori Statistical Uncertainties and Latitude-Temporal Data Distribution

[41] In section 2.3, we considered the statistical uncertainty in each density retrieval, calculated a priori from instrumental uncertainties in the electron flux. We saw in Figure 2e that these uncertainties have a wide distribution with a median of about a factor of 5. When combined with expected real orbit-to-orbit variability in mass densities at these altitudes of factors of 2–3 [*Tracadas et al.*, 2001], we expect standard deviations of roughly an order of magnitude in density retrievals at the same latitude and within a time interval short in comparison to Martian seasons. This is indeed the case, as demonstrated both by example in the width of the distributions shown in Figure 5, and by histogram over the entire data set in Figure 7. Further, Figure 7 shows that the typical standard deviation in density retrievals remains at 0.8–0.9 orders of magnitude independent of the size of the bins in latitude and Ls.

[42] This substantial variability means that a single density retrieval, or even several adjacent retrievals, will tell us very little about the structure and variability of the upper thermosphere. We need to consider temporal and geographic bins large enough that the standard error in the mean density (i.e., standard deviation divided by the square root of the number of data points) becomes small compared to the typical variation between bins. Figure 8 compares two distributions from the same latitude band at opposite ends of the Martian year, between which the average density contrast is highest.

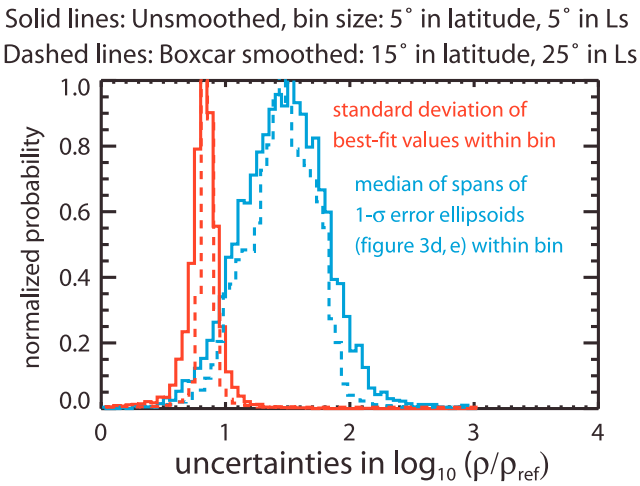

Figure 7. A priori and a posteriori uncertainties across the data set. The red lines are histograms of the standard deviation of values of $\log_{10}[\rho/\rho_{ref}]$ within each bin of latitude and Ls, i.e., an a posteriori measure of uncertainty. The blue lines are histograms of the median of spans in $\log_{10}[\rho/\rho_{ref}]$ of 1-σ error ellipsoids (i.e., twice the a priori estimate of uncertainty) within the same bins. Solid lines represent unsmoothed bin sizes of 5° in latitude and 5° in Ls. Dashed lines represent boxcar-smoothed bins of 15° in latitude and 25° in Ls.

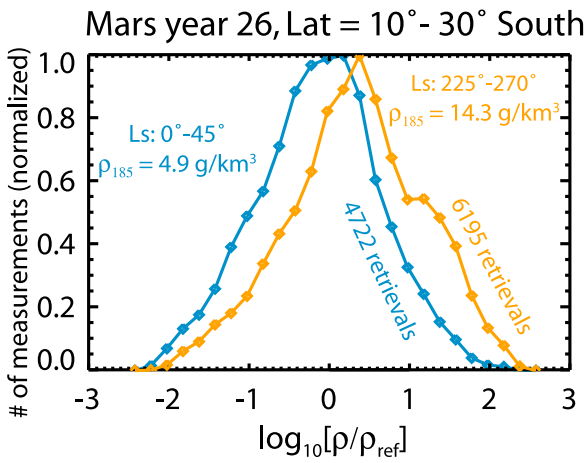

Figure 8. Comparison between distributions of ρ/ρ_{ref} from two different 45° spans of Ls in Mars year 26 (0°–45°, 225°–270°) in the latitude band 10°–30° S, including only data points with magnetic elevation angles greater than 40° and values of B_{185} greater than 15 nT (as discussed in section 2.5).

The difference between the mean values of $\log_{10}(\rho/\rho_{ref})$ of the distributions is ~0.5, approximately half of their standard deviations. However, because of the large number of data points comprising each distribution, their standard errors in $\log_{10}(\rho/\rho_{ref})$ are ~0.02 (corresponding to ~5% in mass density at 185 km). A Kolmogorov-Smirnov test confirms that these distributions represent real variation in the Martian upper thermosphere, with the probability of them being drawn from the same parent distribution at $< 10^{-10}$.

[43] We tested several bin sizes in an attempt to balance latitudinal and temporal resolution with the need to have enough individual density retrievals to ensure sufficiently small standard errors in the mean of each bin. Figure 9 shows data coverage and standard errors for unsmoothed bin sizes of 5° in both latitude and Ls and boxcar-smoothed averages of 15° in latitude and 25° in Ls, which we choose as our preferred way to bin the retrieve the mass densities for interpretation (see Figure 10). We determined, somewhat arbitrarily, that bins with less than 300 measurements (corresponding to a typical uncertainty of ~0.05 in $\log_{10}(\rho/\rho_{ref})$ or ~12% in ρ/ρ_{ref}) should be excluded from interpretation.

[44] The temporal-latitudinal data coverage shown in Figure 9 is explained by three effects. First, the 25.4° tilt of Mars' rotation axis with respect to its orbital axis, coupled with the sun-synchronous orbit of the MGS spacecraft at 2 A.M./2 P.M. local time, means that accessible latitudes with solar zenith angles greater than 113° span approximately 130° and migrate north and south with the Martian seasons. Second, the planet-fixed crustal magnetic fields' position with respect to the solar wind and IMF in Mars Sun-state coordinates, migrates in a similar fashion over the course of the Martian year. Therefore the fraction of the time that a crustal field at a given location will magnetically connect to the external field (i.e., allowing loss cones to form) also varies with season [*Brain et al.*, 2007]. Third, substantial telemetry dropouts, related to spacecraft operations and Mars passing behind the Sun, explain the occasional gaps in data.

4. Results

4.1. Densities at 185 km Over 4 Martian Years

[45] In the absence of direct solar EUV heating, densities and temperatures in the nightside upper thermosphere are controlled largely by cooling (i.e., CO_2 15-micron radiation and thermal conduction) and dynamics (see Figure 10) [*McDunn et al.*, 2010]. Nonetheless, dayside insolation is still the primary source of energy input to the atmosphere as a whole and, as such, we expect it to be a factor in determining nightside conditions. Over time scales of a sol or longer, for a given point on the planet the average solar energy input varies with latitude and solar longitude (Ls), while all geographic longitudes receive the same diurnally averaged insolation. Therefore, we choose to examine how zonally averaged densities vary as a function of latitude and season. As discussed in section 3.3, we require large sample sizes (>300 measurements) to keep statistical errors acceptably low, so it is necessary to use a running average of densities over 25° in Ls (47.7 days, 46.4 sols or 572 orbits) and 15° in latitude, as plotted in Figure 10b. This is especially important away from the equator where data coverage is far sparser. It should be noted that these are not true zonal averages because the data sampling with respect to longitude is not regular, but follows the pattern shown in Figure 6a.

4.2. Comparison With External Factors

[46] As mentioned above, we can expect cooling and dynamics to play a very substantial role in determining upper thermospheric densities at 2 A.M. local time. It is nonetheless instructive to make comparisons with external factors that may play at least an indirect role in affecting nightside upper thermospheric densities.

4.2.1. Dayside Solar UV Flux

[47] Solar ultraviolet (UV) flux on the dayside in the wavelength range 20–200 nm directly heats the upper atmosphere. Altitudes of peak UV absorption by CO_2 (i.e., optical depth of unity) are wavelength-dependent. 20–110 nm UV radiation is absorbed mostly over the altitude range 120–135 km. A substantial fraction of the flux in this range comes from the 30.6 nm Helium II line, which is thus an adequate proxy for heating at these altitudes [*Paxton and Anderson*, 1992]. 120.6 nm Lyman-α is easily the brightest line in the solar UV and causes peak heating in the 60–70 km range. 135–160 nm UV causes peak heating around ~90 km altitude and well-represented by the Carbon IV line at 154.9 nm [*Paxton and Anderson*, 1992]. Solar irradiance in these 3 lines (He II,C IV and Ly-α) from the Solar Extreme ultraviolet Monitor (SEM) on board the Solar and Heliospheric Observatory (SoHO) spacecraft [*Judge et al.*, 2000] and the Solar Extreme ultraviolet Experiment (SEE) onboard the Thermosphere Ionosphere Mesosphere Energetics and Dynamics (TIMED) spacecraft [*Woods and Eparvier*, 2006] instruments, have been scaled and phase-shifted to Mars and plotted above the retrieved densities in Figure 10a for comparison. The wavelength bins over which these irradiance curves have been calculated are not the same width and so the absolute magnitudes of the curves should not be compared with one another. Rather, since each line primarily affects a

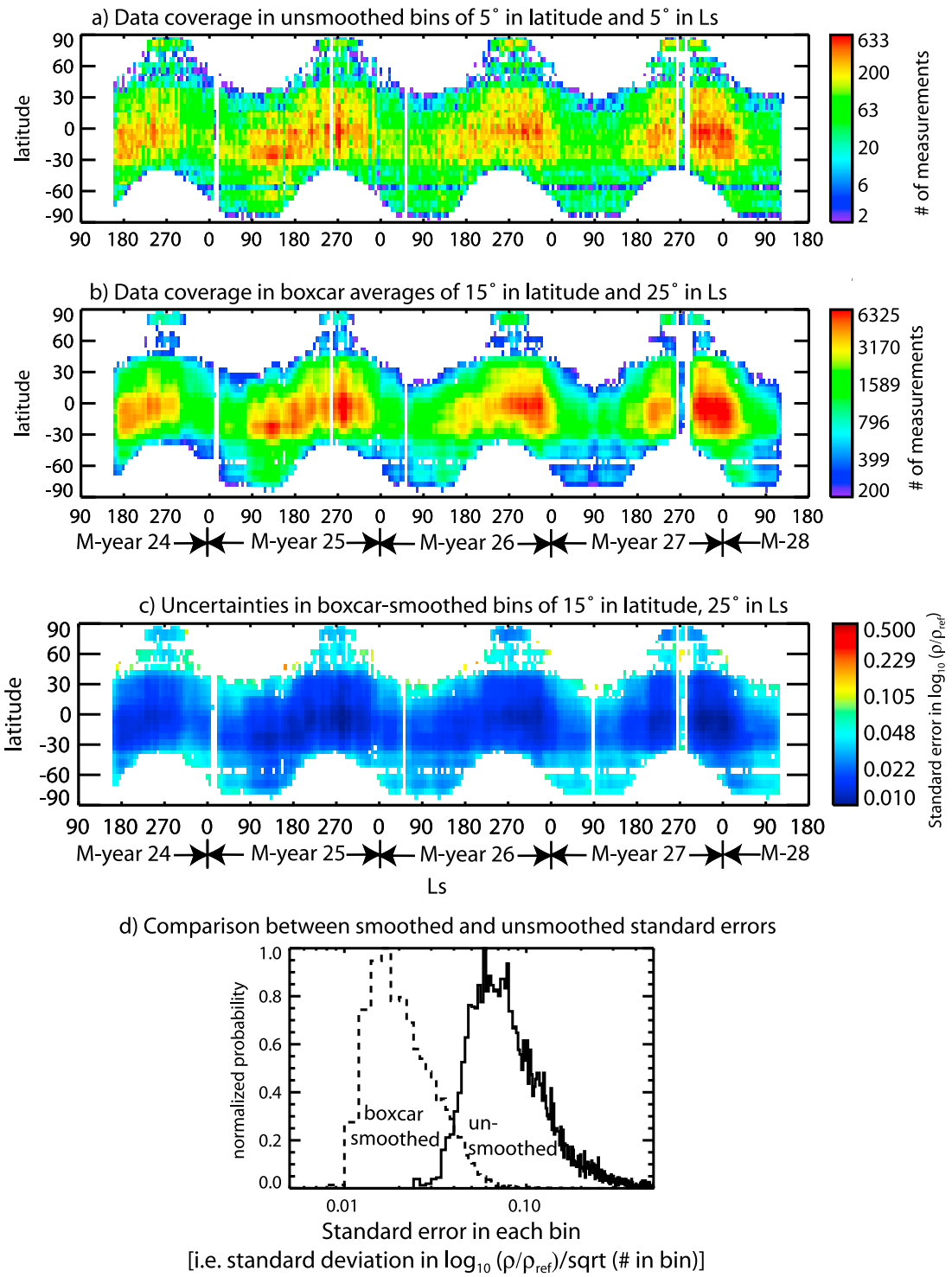

Figure 9. Data coverage and uncertainties with respect to Ls and latitude over the entire MGS mapping mission from April 1999 until November 2006. (a) The 'raw' data coverage in latitude bins of 5° and temporal bins of 5° of Ls (year-averaged equivalent of 9.5 Earth days, 9.3 sols or 115 MGS orbits). (b) The data coverage in the smoothed latitude and Ls bins (25° and 15°, respectively) used to construct the primary results of this paper, i.e., Figure 10b. (c) The standard error in $\log_{10}[\rho/\rho_{ref}]$ (i.e., standard deviation divided by the square root of the number of data points) in the smoothed bins. Individual 5° × 5° bins with fewer than 10 measurements are not considered. (d) Compares histograms of this standard error for the unsmoothed (solid line) and boxcar-smoothed (dashed line) bins.

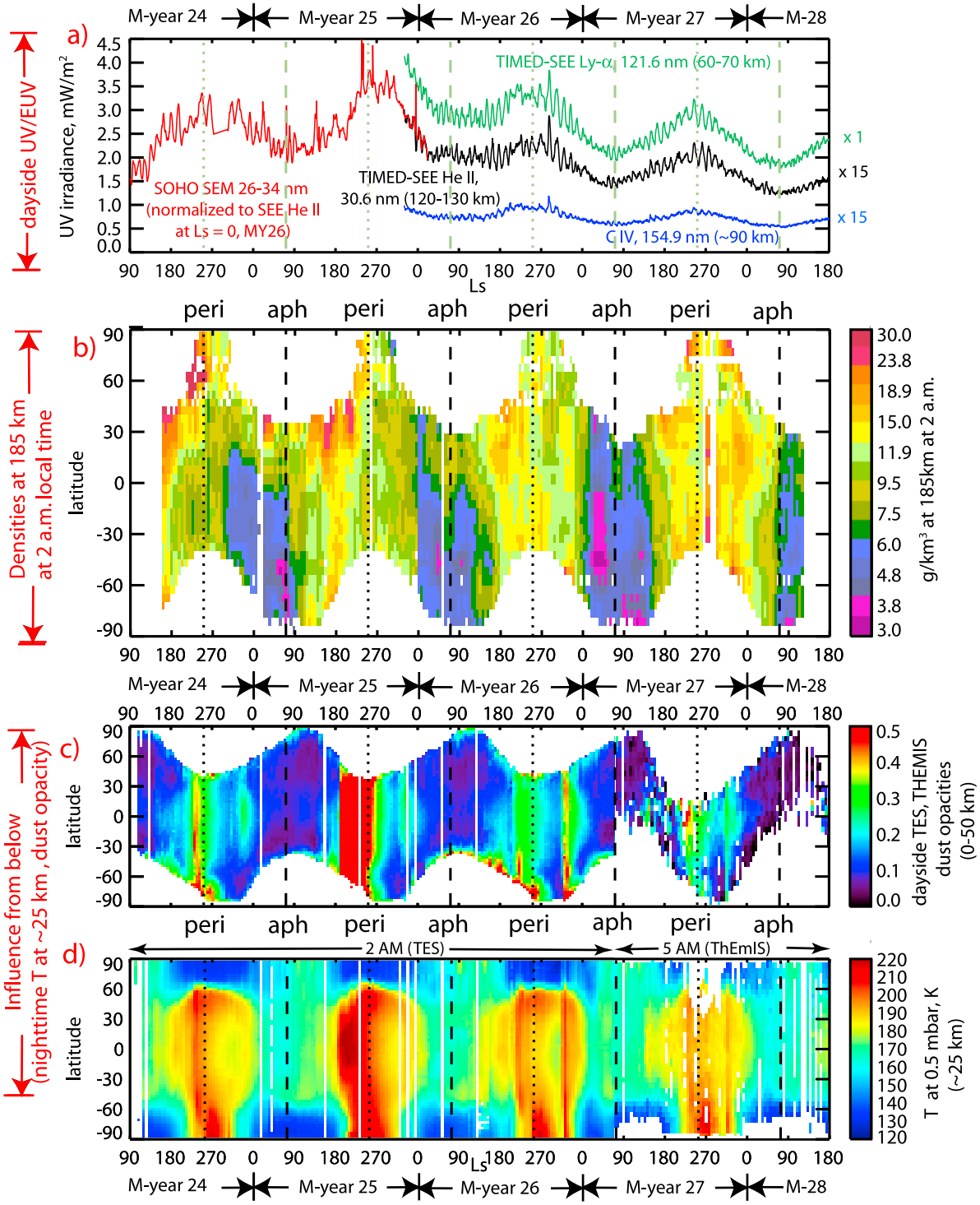
M-year 24
M-year 25
M-year 26
M-year 27
M-28
a)
dayside UV/EUV
UV irradiance, mW/m²
TIMED-SEE Ly-α, 121.6 nm (60-70 km)
x 1
x 15
TIMED-SEE He II, 30.6 nm (120-130 km)
SOHO SEM 26-34 nm (normalized to SEE He II at Ls = 0, MY26)
C IV, 154.9 nm (~90 km)
x 15
Ls
peri
aph
b)
Densities at 185 km at 2 a.m. local time
latitude
g/km³ at 185km at 2 a.m.
c)
Influence from below (nighttime T at ~25 km, dust opacity)
dayside TES, THEMIS dust opacities (0-50 km)
d)
2 AM (TES)
5 AM (ThEmIS)
T at 0.5 mbar, K (~25 km)

Figure 10

different range of altitudes in the Mars atmosphere, we wish to concentrate on the temporal variation within each line.

[48] Excluding the regular annual variations in UV fluxes due to Mars' changing heliocentric distance, we see no clear evidence of an overall multiyear decrease in densities to accompany the decrease of 30–50% in Lyman-α and He II fluxes from solar max in Mars year 25 to near solar min in Mars year 27/28 (The 154.9 nm line varies by only ~15% as it is closer to the less variable near-UV). Given the efficiency for downward transport by thermal conduction and given that the upper thermosphere at 185 km at 2 A.M. is 50–125 km above and more than 8 h removed from this dayside UV heating, this lack of correlation is not surprising.

4.2.2. Nightside Lower Atmospheric Temperatures and Dust Opacity

[49] Densities and temperatures in the nightside lower atmosphere (below ~50 km) are affected by daytime heating by solar infrared (IR) radiation and by dust activity which is caused, primarily during the perihelion/southern summer season, by that same heating. Atmospheric dust absorbs solar radiation and heats the air in which it is suspended (the year 25 dust storm increased temperatures at 25 km altitude by > 50° K [*Smith et al.*, 2002]), thereby increasing scale heights and hence densities at altitudes above the dust. Dust loading affects densities at least as high as the lower thermosphere; e.g., densities at 126 km increased by a factor of ~3 during the Noachis the storm of 1997 [*Keating et al.*, 1998], and the effect of dust events over the densities in the lower thermosphere has been shown in SPICAM data [*Forget et al.*, 2009]. In contrast, there is no published data showing the effects of substantial dust loading above ~140 km [e.g., *Tolson et al.*, 2007]. It is worth noting that, at approximately twice the altitude, *Forbes et al.* [2008] found that neutral densities at 390 km do not detectably depend on dust activity.

[50] We choose to plot (1) dayside dust opacity (from the Thermal Emission Spectrometer (TES) on MGS and Thermal Emission Imaging Spectrometer (THEMIS) on Mars Odyssey) [*Smith*, 2004, 2009] and (2) nighttime temperatures at the 0.5 mbar pressure level (or ~25 km altitude) as measured by the TES instrument at 2 A.M. local time and the THEMIS instrument at 5 A.M. local time [*Smith et al.*, 2001; *Smith*, 2004] in Figure 10d. Examining these 2 panels, there is a strong correlation apparent between dust opacity and nightside temperatures at 0.5 mbar.

[51] We find that, at latitudes equatorward of 40° north and south, there does appear to be a rough correlation between lower atmospheric temperature and upper atmospheric density, at least in Mars years 25 and 26. In particular notice the feature around Ls ~310°, MY26, where there is a dip in lower atmospheric temperatures in between 2 major dusty periods and where densities at 185 km also fall (by ~30%). However, while lower atmospheric temperatures in the winter polar night are quite similar between the North and South hemispheres (~130° K), there is a huge difference between corresponding densities in the upper thermosphere. This asymmetry between the winter hemispheres in the north and south may be due to strong interhemispheric circulation [*Bougher et al.*, 2006] and will be discussed further in the following sections. The response to the 2001 global dust storm will also be discussed separately.

4.3. Repeating Features Connected to Seasonal Insolation Changes

[52] Some features in the 2 A.M. neutral density at 185 km approximately repeat each Martian year. First, we observe, and expect, densities to be broadly higher near perihelion and lower near aphelion, since lower atmospheric temperatures are generally warmer and the solar flux is 45% higher at the former compared with the latter. This is particularly true at southern midlatitudes where densities vary by a factor of ~7 from perihelion/summer to aphelion/winter. Second, at aphelion, densities are lower in the southern (i.e., winter) hemisphere than in the northern (summer) hemisphere. The converse is not found to be the case, with densities fairly constant with latitude near perihelion (except perhaps for Mars year 24 when high latitude northern (winter) hemisphere densities are actually higher than equatorial densities). This asymmetry has also been observed in MGS and Odyssey accelerometer-derived densities and temperatures in the lower thermosphere (100–130 km altitude) [*Keating et al.*, 2003; *Bougher et al.*, 2006] and is consistent with accelerometer measurements from the MRO spacecraft, which was aerobraking with periapsis in the southern winter polar night at that time [*Bougher et al.*, 2007; *Keating et al.*, 2006].

[53] We attribute this asymmetry between the winter hemispheres to stronger interhemispheric circulation during northern winter, which is driven by stronger insolation and dust heating near perihelion compared with aphelion, resulting in subsidence, adiabatic heating and resulting warmer temperatures (and elevated densities) in the northern polar night. MTGCM simulations support this interpretation, displaying adiabatic heating rates typically between 3 and 10 times higher for the North winter pole compared to the South winter pole [*Bougher et al.*, 2006] at lower thermosphere altitudes (~120 ± 20 km). The inter-hemispheric circulation giving rise to this warming is predicted by both the MTGCM and the LMD-MGCM [e.g., *Bougher et al.*, 2006; *González-Galindo et al.*, 2009], but has not been confirmed by any independent wind measurements. Densities at 185 km respond to this lower thermosphere heating through expansion of the

Figure 10. Primary results. (a) The solar UV irradiance from 2002 onwards from the TIMED-SEE experiment [*Woods and Eparvier*, 2006] in 3 important bands for atmospheric heating: Lyman-α (green line), Helium-II (black line) and Carbon-IV (blue line) centered at wavelengths of 121.6 nm, 30.6 nm and 154.9 nm respectively, causing peak heating at altitudes of 60–70 km, 120–130 km and ~90 km respectively. Shown in red is UV irradiance in a band from 26 to 34 nm measured by the SOHO SEM instrument [*Judge et al.*, 2000] constructed from 27-day averages with solar flares removed, normalized to match the TIMED-SEE data. All 4 curves have been scaled and phase-shifted from 1AU to Mars' position. (b) Neutral mass density at 185 km above the areoid, zonally averaged and plotted as a function of latitude and Ls, boxcar smoothed over 15° in latitude and 25° in Ls. Individual 5° × 5° bins with fewer than 10 measurements are not considered. (c) Mean dayside dust opacity. (d) Nighttime temperatures in the lower atmosphere (pressure level 0.5 mbar or ~25 km altitude) measured at 2 A.M. and 5 A.M. local time by the MGS TES and Odyssey THEMIS instruments, respectively [*Smith*, 2004, 2009].

local atmospheric column above ~100 km. This results in the elevation of the altitude of constant density levels in the upper thermosphere. Equivalently, this yields enhanced densities at constant altitudes above ~100 km with respect to those without winter polar warming. Therefore, the repeating features in the Mars nighttime upper thermosphere (~185 km) can at least be qualitatively understood based on theory.

4.4. Interannual Changes

[54] Mars' obliquity and eccentricity control how the solar flux impacting a given latitude changes over the Martian year, and hence are expected to control the gross, annually repeating features observed in temperatures and densities at least up to the exobase where solar wind interaction and atmospheric escape become important. However, we observe substantial interannual variability in nightside upper thermospheric densities. Directly or indirectly, this variability is likely linked to interannual changes in solar EUV and dust loading (which drives temperatures) in the lower atmosphere. We now discuss some of the more interesting interannual variations in our retrieved densities.

4.4.1. Shifting of Southern Winter Low Density Period

[55] Each year we observe a sharp decrease in average density at 185 km of a factor of ~2 from above 10 g/km^3 to below 5 g/km^3 at all observable southern latitudes sometime during southern autumn. For latitudes between ~10°S and 40°S, this decrease occurs around Ls ≈ 300° in Mars year 24 but does not occur until Ls ≈ 350° (~3 months later) in years 25/26 and 26/27. In year 27/28, there is a gradual decrease beginning around Ls 0° but it does not fall sharply (as in the other years) until Ls ~60°. For the winter of year 24/25, the minimum at these latitudes is reached by Ls ≈ 330°, whereas in years 25/26 and 26/27, the minimum does not occur until ~100 days later at Ls ≈ 30° and for year 27/28 it occurs even later at Ls ≈70°. In addition, for southern latitudes poleward of 50°S, the minimum occurs around Ls ≈ 30° in the first 3 years but not until Ls ≈ 70° for the winter of year 27/28.

[56] Also each year, at some time following the solar flux minimum at aphelion (Ls = 70°), nightside thermospheric densities at 185 km at all observed latitudes begin to increase, reaching a maximum around Ls = 180°, corresponding to increasing temperatures in the lower atmosphere [*Smith*, 2004]. However, just as with the decrease preceding it, the timing and character of this increase also varies substantially between years. In year 25 this increase is fully underway at all latitudes by Ls ≈ 80°, though generally steeper for more poleward southern latitudes, while less pronounced at the equator and northern hemisphere. In year 26 however, the increase begins around Ls ≈ 90° near the equator and northward, while the densities stay low until Ls ≈ 120° before rising for latitudes southward of 15°S. In year 27, again the equator and observable northern latitude densities increase before those in the southern hemisphere, but in this case the density increase at all latitudes is delayed by an additional ~20° of Ls compared with year 26. This year 27 density increase at 185 km was by a factor of ~3, similar to the increase observed almost simultaneously at 70–130 km on the night side by the SPICAM instrument [*Forget et al.*, 2009].

[57] It is indeed remarkable that the beginning of this southern winter density low varies by ~90°–120° of Ls, while its end varies by ~60°–80°. It would appear that the low is shifting later as the solar cycle progresses from solar max to solar min. Since the mean overall densities are not decreasing as the solar EUV flux ramps down, this phenomenon of the shifting density low may be partially due to changes in seasonal dynamics as the dayside thermosphere receives progressively less EUV each year at the beginning of southern autumn (Ls ≈ 300°–0°).

[58] It is also possible that interannual changes in dust distribution may be contributing to the shifting density low. Although the first part of the lower atmosphere dusty season in southern autumn ends just after perihelion around Ls ≈ 285° each year, there is a second wave of dust activity (and associated lower atmosphere heating) which peaks around Ls ≈ 330°. This second wave is progressively stronger and longer-lasting in years 24, 25 and 26 while decreasing somewhat in year 27. It may be that the weaker 2nd wave of dust in year 24 contributed to the winter low in nightside upper thermospheric densities occurring earlier compared with subsequent years when that second wave was stronger and persisted somewhat later in the season. However, dust cannot be the entire story here since the atmosphere is almost completely dust-free during the post-aphelion density increase (which also shifts later as the solar cycle progresses). In addition, the "muted" or unclear response to densities at 185 km to the 2001 global dust storm (section 4.4.4) lends further weight to dust not being the primary factor controlling this phenomenon.

4.4.2. Local Density Maxima At/Near Aphelion

[59] In years 26 and 27, at equatorial and low southern latitudes, we observe a small but detectable (~20–30%) increase in density, spanning ~50° of Ls and occurring almost exactly at aphelion. In year 25 there may be an equivalent increase ~20° of Ls before aphelion, but not nearly as robust as years 26 or 27. There is a strong 'hint' of a similar increase in year 28, though centered 20°–30° of Ls after aphelion. Unfortunately, the termination of the data set at Ls = 120° precludes any definitive judgments.

[60] The geographically limited area of this increase (typically within 20°–30° of the equator) suggests a change in the circulation pattern near aphelion. As for the interannual variability therein, as with the later start of the post-aphelion density increases (previous subsection), perhaps the reason for the interannual differences in the local maxima is related to the overall decreasing solar EUV flux from year 25 through year 28, though this is largely conjecture.

4.4.3. Unexpected Densities at 185 km During the 2001 Global Dust Storm

[61] Dust storms have been shown to have substantial effects in the lower and middle thermosphere, for example, at ~125 km during the 1997 Noachis regional dust storm [*Keating et al.*, 1998]. In contrast, the planet-encircling 2001 global dust storm during Mars year 25 [*Smith et al.*, 2002] did not cause any substantial rise in densities at 185 km that was significantly larger in intensity compared with other years. In fact, as also reported by *Lillis et al.* [2008a], densities in the southern hemisphere appear to reach their maximum around Ls = 180°, just before/as the dust storm starts, then slowly decrease during the dust storm. One possible explanation for this onset/decay of densities (seemingly unrelated to dust opacity variations) may be related to the time-evolution of the dust driven

inter-hemispheric circulation. As dust opacities first ramp up, southern hemisphere (SH) local temperatures and densities increase, causing the circulation to intensify throughout the lower atmosphere (<100 km), resulting in a related enhancement of northern hemisphere (NH) temperatures and densities. As the season progresses, the increasing solar EUV-UV fluxes intensify the thermospheric circulation (>100 km), providing greater upwelling in the SH and local cooling (and decreased densities). Meanwhile, further enhanced lower atmosphere dust driven transport also cools temperatures and elevates NH temperatures (and densities) in concert with the thermospheric circulation (doubled effect). Dust storm evolution simulations linking the lower and upper atmospheres are needed to evaluate these dynamical explanations.

[62] Alternatively, since there is no definitive (clearly strong) correlation with dust activity elsewhere in the data set, another possibility may be that dust in the lower atmosphere (<60 km [*Smith*, 2004, 2009] is not a dominant influence on densities at 185 km, near and just above the exobase. As noted earlier, *Forbes et al.* [2008] found that neutral densities at 390 km do not seem to depend on dust activity.

5. Comparisons With Two Global Circulation Models

[63] Though the measurements shown in Figure 10 are useful by themselves in elucidating trends in the Martian upper thermosphere/lower exosphere, they are also useful in guiding the development of global circulation models (GCMs) of the entire Martian atmosphere. Comparisons between observations and these models can give clues as to which physical processes need to be incorporated in order to increase the accuracy of the models, output from which forms the basis for planning mission-critical aerobraking and entry-descent-landing (EDL) operations.

[64] The two models to which we shall compare our results are: the United States-based Mars Global Circulation Model-Mars Thermospheric Global Circulation Model (MGCM-MTGCM or simply MTGCM for brevity) framework and the France-based Laboratoire de Météorologie Dynamique Mars Global Circulation Model (LMD-MGCM). They are briefly summarized below before comparisons are examined.

5.1. Coupled MGCM-MTGCM Framework

[65] The MTGCM is a finite difference primitive equation model that self-consistently solves for time-dependent thermospheric neutral temperatures, neutral-ion densities, and neutral winds over the Mars globe. The modern MTGCM code [e.g., *Bougher et al.*, 2004, 2006, 2009; *Bell et al.*, 2007] contains time-evolving equations for the major neutral species (CO_2, CO, N_2, and O), selected minor neutral species (e.g., Ar, O_2), and several photochemically produced ions (e.g., O_2+, CO_2+, O+, and NO+) and electrons below 180 km. These composition, temperature, and 3- component wind fields are calculated on 33 pressure levels above 1.32 mbar, corresponding to altitudes from roughly 70 to 300 km (at solar maximum conditions), with a 5 degree resolution in latitude and longitude. The vertical coordinate is log pressure, with a vertical spacing of 0.5 scale heights. Key adjustable parameters which can be varied for MTGCM cases include the F10.7 or E10.7-cm index (solar EUV-UV flux variations over 2.4–225.0-nm), the heliocentric distance and solar declination corresponding to Mars seasons. A fast non-Local Thermodynamic Equilibrium (NLTE) 15-micron cooling scheme is implemented in the MTGCM, along with corresponding near-IR heating rates [e.g., *Bougher et al.*, 2006]. The feedback of simulated atomic O upon CO_2 cooling rates is important, and is included. These inputs are based upon detailed 1-D NLTE model calculations for the Mars atmosphere [e.g., *López-Valverde et al.*, 1998].

[66] The MTGCM is driven from below by the NASA Ames Mars MGCM code at the 1.32-mbar level (near 60–80 km) [*Bougher et al.*, 2004, 2006, 2009]. In other words, key variables are passed upward from the MGCM to the MTGCM at the 1.32-mbar level at every MTGCM grid point on 2-min time steps: temperatures, zonal and meridional winds, and geopotential heights. This detailed coupling allows both the migrating and non migrating tides to cross the MTGCM lower boundary and the seasonal effects of the expansion and contraction of the Mars lower atmosphere to extend to the thermosphere. No downward coupling is presently activated between the MGCM and the MTGCM. However, the impact of lower atmosphere dynamics upon the upper atmosphere densities and temperatures is significant [*Bell et al.*, 2007].

[67] The NASA Ames General Circulation Model (MGCM), which provides the lower boundary for the coupled MGCM-MTGCM simulations, is a primitive-equation finite difference (time and space) numerical grid point model of the Martian atmosphere [e.g., *Haberle et al.*, 1999]. The model employs a terrain following "sigma" (normalized pressure) coordinate in the vertical, in which 26–30 model layers extend to an altitude of ~90 km (~0.00005 millibars) above the reference 'aeroid' defined by MOLA (1x1°) data [e.g., *Smith et al.*, 2001]. The MGCM code has recently undergone numerous improvements in the treatment of various physical forcing processes which drive the atmosphere's thermal and dynamical states. For example, the MGCM can now be run with active dust lifting, with surface stress [*Newman et al.*, 2005; *Haberle et al.*, 2003] and dust devil-dependent dust lifting [*Newman et al.*, 2002] both being incorporated in the model. The model's dynamical core (including tracer transport) solves the atmospheric thermodynamic equations on a 5° latitude × 6° longitude Arakawa C-grid [*Suarez and Takacs*, 1995]. The suspended dust opacity (empirically prescribed for our cases) is employed for the radiative heating calculation within the correlated-k radiative transfer routine covering 12 spectral bands tailored for the Mars CO_2/water vapor atmosphere covering the range of 0.3 to 250 microns.

5.2. Ground-to-Exosphere LMD-MGCM

[68] The LMD-MGCM solves the primitive equations of hydrodynamics on a sphere, using a grid point discretization. The radiative balance accounts for the effect of CO_2 and suspended dust.

[69] A realistic CO_2 condensation scheme is included, essential for a good simulation of the surface pressure annual cycle. A water cycle [*Montmessin et al.*, 2004] and a photochemical model for the lower atmosphere [*Lefevre et al.*, 2004] have also been included in the model. A

number of subgrid scale processes near the surface are considered, in particular the boundary layer turbulence, convection, relief drag and gravity wave drag. Surface processes are accounted for by including MOLA topography and TES thermal inertia. In its current version, 14 chemical species are included in the model: CO_2, CO, $O(^3P)$, $O(^1D)$, O_2, O_3, H, OH, HO_2, H_2, H_2O, H_2O_2, N_2 and Ar. All of them undergo transport by the general circulation, as well as by molecular diffusion. N_2 and Ar are treated as chemically inert, while all the other species are affected by chemistry.

[70] To extend the validity of the LMD-MGCM up to the thermosphere, parameterizations for the following physical processes were also included: NLTE corrections to the CO_2 IR radiative balance, UV heating, thermal conduction, molecular diffusion and a photochemical model appropriate for the upper atmosphere [*Angelats i Coll et al.*, 2005; *González-Galindo et al.*, 2005, 2009]. Note that for the treatment of the cooling by 15-micron cooling, the same scheme than in the MTGCM is used, based on *López-Valverde et al.* [1998]. However, the effects of variable atomic oxygen in this process are not taken here into account, which as explained by *Forget et al.* [2009] produces an underestimation of this cooling term.

5.3. Direct Comparison Between Retrieved Densities at 185 km and GCM Results

[71] For the most meaningful possible comparison, we retrieved from the LMD-MGCM and MTGCM 2-dimensional maps of mass density at 185 km above the reference areoid as a function of latitude and longitude at a fixed local time of 2 A.M. Due to the computationally intensive nature of the simulations and the slightly different ways in which the two models are run and the results recorded, comparisons were made in the following way:

[72] 1. MAG/ER: densities were binned by latitude intervals of 15° (e.g., 90°–75°S, 75°–60°S etc.) and for ranges of Ls = 90°–120°, 120°–150°, 150°–180°, 180°–210° and averaged across all longitudes within those latitude and Ls bins for Mars years 24–28.

[73] 2. LMD-MGCM: average latitude-longitude density maps were extracted from 20-sol static runs (i.e., Ls did not advance during the run) for ranges of Ls = 90°–120°, 120°–150°, 150°–180°, 180°–210° from model runs with appropriate lower atmospheric dust opacities (as measured by MGS TES) corresponding to Mars years 24, 25 and 26, with a constant EUV flux appropriate for solar average conditions. This flux should be appropriate for the Ls = 90–210 interval for MY24 and 25, but probably too high for MY26 (see Figure 10a). Of course, the solar flux changes with heliocentric distance.

[74] 3. MTGCM: average latitude-longitude density maps were extracted from 30-sol static runs (i.e., Ls did not advance during the run) for Ls = 90°, 120°, 150°, 180° and 210° and appropriate solar EUV flux and dust opacities from Mars years 24–28. Specifically, adopted solar fluxes range from solar high (MY25) to solar low (MY27). Dust opacity data sets were taken from MGS TES mapping seasons #1, 2, and 3 and Odyssey THEMIS mapping season #1, corresponding generally to MY24, 25, 26 and 27, respectively. Density maps with adjacent values of Ls were then averaged together, i.e., Ls = 90° and Ls = 120° were averaged to approximate Ls = 90°–120°.

[75] For each year and Ls range, LMD-MGCM and MTGCM densities from the latitude-longitude maps were weighted by the geographic locations of the individual MAG/ER data points within each of the aforementioned latitude intervals of 15°. Thus we have attempted to compile the most appropriate 'apples-to-apples' comparison between MAG/ER densities and those from the LMD-MGCM and the MTGCM. This comparison is shown in Figure 11. There is not a perfect overlap between the available runs from the two models in terms of Ls and Mars year, nor is the range of Ls nearly complete. However, a comprehensive and detailed comparison is outside the scope of this paper, the primary objective of which is to explain the extension of the ER density probing technique and present the mass density data.

5.4. Discussion of MAG/ER-LMDMGCM-MTGCM Comparisons

[76] It should be noted from the outset here that the nightside upper thermosphere is likely controlled by dynamical processes (i.e., global circulation, tides, gravity waves), which are 1-step removed from solar UV forcing, This alone makes GCM modeling of nightside densities a very difficult business. That said, some confidence can be taken from the fact that the two models do a reasonably good job of bracketing the observations, as can be seen in Figure 11.

[77] Overall, the simulated density levels (for both MTGCM and LMD-MGCM models) increase regularly with the advance of the seasons (Ls = 90° to 210°) for each Martian year. This occurs irrespective of the solar flux conditions specified and the dust opacities. This is a heliocentric distance effect, a response by the upper atmosphere densities to steadily increasing lower atmosphere IR heating as the annual march from aphelion toward equinox seasons occurs. These simulations do not cover a very wide range of Ls; yet, the trend does match that of the MSG/ER derived densities (see Figure 10b).

[78] The inter-annual variations illustrated in Figures 10b and 10c suggest only a weak correlation between dust loading and nightside densities at 185 km (near the exobase). What do the models reveal? MTGCM simulations were conducted for solar moderate conditions for MY 24 and 26. LMD simulations were conducted for solar moderate conditions throughout all seasons. When choosing to compare Ls = 150–210 panels only (those corresponding to the largest potential changes in lower atmosphere dust opacities from year-to-year), we see the following:

[79] 1. MTGCM simulations (MY 24 and 26) reveal a very similar magnitude and latitude variation of densities at 185 km. Therefore, no significant differences are seen due to dust opacity variations alone.

[80] 2. LMD (MY 24, 25, 26) simulations show equatorial densities for MY25 and MY26 that are elevated by $\leq 50\%$ compared to MY24 for the Ls = 180–210 panels. A weak variation of densities at 185 km is seen between MY24, MY25, and MY26.

[81] 3. Together these initial model results suggest that the nightside densities at 185 km should not be strongly dependent upon lower atmosphere dust loading and its variations from year to year. This is consistent with MGS/ER densities illustrated in Figure 10b.

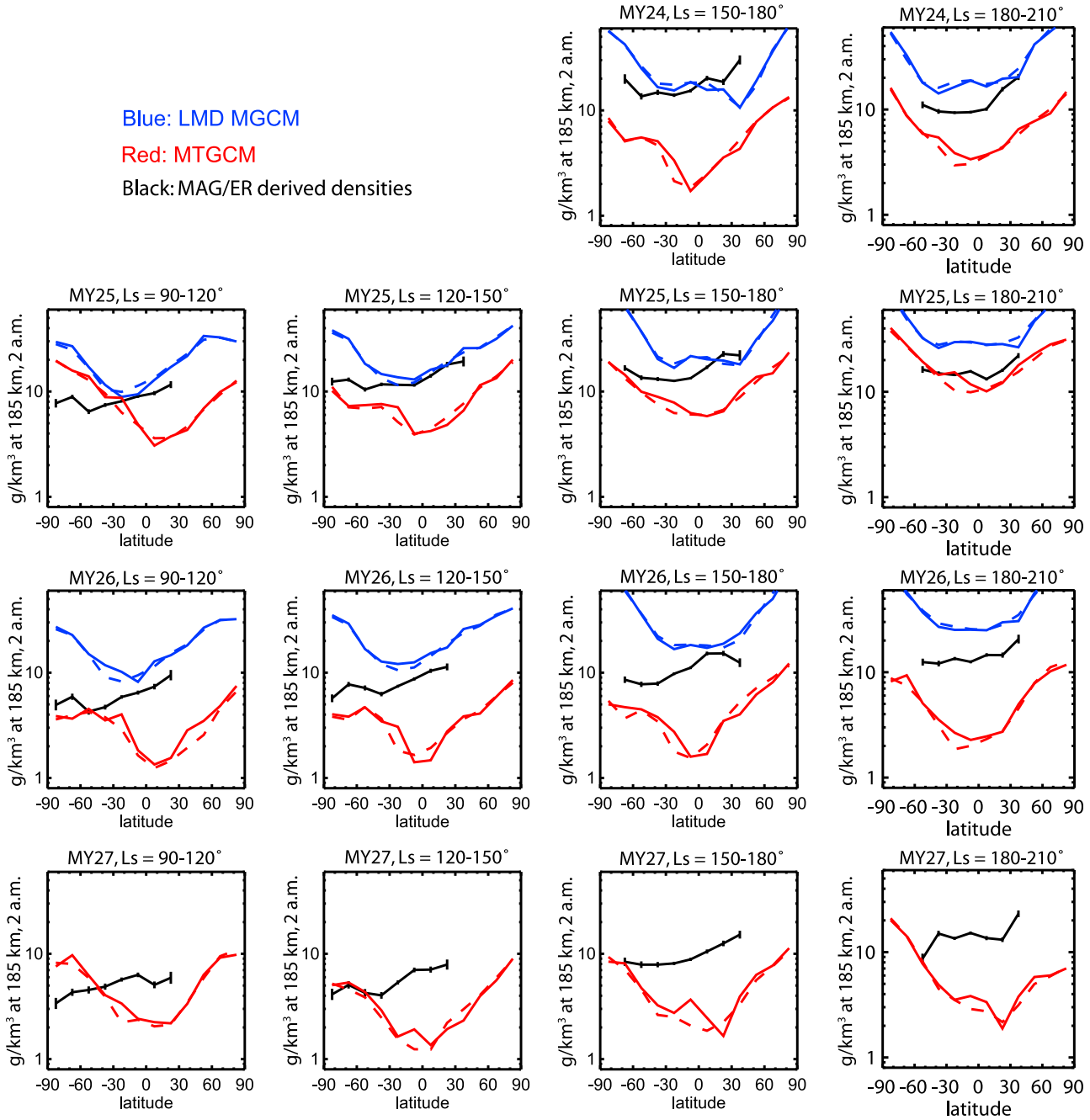

Figure 11. Comparison of ER-derived densities at 185 km with results from the MTGCM (red lines) and LMD GCM (blue lines). The solid lines represent model results weighted appropriately according to the location of the ER data points, while the dashed lines represent simple zonal averages. The rows represent different Mars years, while the columns represent different ranges of Ls. See you section 5.3 for a more detailed explanation.

[82] In addition, Figures 10a and 10b suggest only a weak correlation between solar UV fluxes and nightside densities at 185 km (near the exobase). What do the models reveal? Panels for a constant season and consistently low dust loading (Ls = 90–120;120–150) should be compared to focus upon the solar flux response. MTGCM simulations show equatorial densities at 185 km that noticeably decrease from MY25 to MY26 (~50%), and remain unchanged from MY26 to MY27. This is a rather weak response compared to the factor of ~3 variation of nightside densities with the advance of the seasons (aphelion toward perihelion) and polar warming toward high winter latitudes during perihelion. Again, this weak solar UV response is not surprising, given the direct importance of dynamics and cooling on the Mars nightside, and the indirect role of dayside UV heating.

[83] Overall, the highest simulated densities (for both MTGCM and LMD-MGCM) are revealed for Ls = 180–210 and MY25 conditions. The is partially a heliocentric distance

effect (lower atmosphere expansion with the seasons), and partially a response to MY25 dust opacities (further lower atmosphere expansion). The LMD code indicates this is not a solar UV flux effect; while the MTGCM needs to be re-run (for solar moderate conditions) to confirm this weak solar UV response.

[84] Upon initial comparison of the models, it is clear that the LMD-MGCM tends to overestimate the densities during most of the seasons (especially during Ls = 195° for all three Mars years and during year 26 for all considered values of Ls), while the MTGCM shows the opposite tendency. The primary reason for this discrepancy lies in the fact that the simulated MTGCM nightside [O] densities are used to calculate CO_2 15-micron cooling (dynamic cooling) while prescribed [O] densities are used for the LMD-MGCM (static cooling). This provides stronger CO_2 cooling within the MTGCM than the LMD-MGCM code; cooler thermospheric temperatures result, as well as reduced nightside densities at 185 km. In fact, the transport of MTGCM dayside-created [O] atoms to the nightside accelerates this cooling effect further (Figure 10).

[85] Previous work [*Forget et al.*, 2009] has already shown a similar overestimation of the LMD-MGCM predicted densities when compared to the lower thermospheric (z < 130 km) densities measured by SPICAM during MY27 using the stellar occultation technique. This overestimation was also attributed to the constant atomic oxygen used in the CO_2 15-micron cooling parameterization. However, when the CO_2 cooling scheme of the LMD-MGCM code is modified to include the feedback of simulated [O] on the CO_2 cooling calculation, an average ~3-fold drop in equinox densities at 185 km is realized over all latitudes. This variation is similar to the difference of the LMD-MGCM and MTGCM densities for the Ls = 180–210 season for MY25 conditions. Therefore, a large fraction of the differences between the nightside densities given by these GCM codes (see Figure 9) can be attributed to this "static" versus "dynamic" implementation of the CO_2 cooling scheme in the LMD-MGCM and MTGCM codes, respectively. Nevertheless, an improved NLTE CO_2 cooling scheme is needed for implementation within Mars upper atmosphere GCMs than enables both accurate and "dynamic" CO_2 15-micron cooling rates to be calculated.

[86] Due to a paucity of magnetic anomalies at high northern latitudes, the MAG/ER data set does not adequately cover winter polar conditions at high Northern latitudes, where we expect significant winter polar warming features (and enhanced densities) to emerge (although the sparse MAG/ER data hints at this feature). However, the opposite winter pole (in the Southern Hemisphere) is observed and modeled. Comparisons suggest that although south winter polar warming (i.e., Southern high latitudes near Ls = 105°–135°) should be weak, observed MGS-ER densities generally decrease into this winter polar region from mid-low latitudes, suggesting that this polar warming is even weaker than modeled. Neither model captures this phenomenon well. This may reflect too strong inter-hemispheric thermospheric circulations in both of the models at this season.

[87] A weaker inter-hemispheric circulation is also consistent with other recent data-model comparisons. In particular, MTGCM comparisons with nightside temperatures measured by SPICAM during MY27 indicate that dynamical heating terms are too strong, and simulated temperatures too warm near the mesopause [*McDunn et al.*, 2010]. It is suggested that the MTGCM lacks a realistic formulation of gravity wave drag and dissipation that would serve to slow inter-hemispheric winds and damp tidal amplitudes in the Mars upper atmosphere. For the present study, the deep equatorial troughs of MTGCM-simulated densities at 185 km may be due to simulated upward propagating tidal amplitudes (e.g., diurnal Kelvin wave) that are unrealistically large [cf. *Forbes et al.*, 2002]. In short, some wave momentum deposition mechanism providing drag on the inter-hemispheric winds and tides may be missing in both models.

6. Conclusions

[88] In this paper we have presented a natural extension of the method of *Lillis et al.* [2008a], wherein the shapes of superthermal electron loss cones measured in near-Mars orbit can be fitted with an electron transport model in order to constrain neutral mass densities at 2 A.M. local time at a mean altitude of 185 km, ~20 km above the expected exobase altitude [*Valeille et al.*, 2009a]. We have presented these density measurements over a period of almost 4 Martian years from April 1999 until November 2006, or MY24/165° until MY28/120°. We find the following notable features:

[89] 1. The expected overall expansion and contraction of the upper thermosphere with heliocentric distance, particularly in the southern hemisphere whose shorter, hotter summer coincides with perihelion.

[90] 2. Densities decrease toward the south pole in southern winter, but not toward the north pole in northern winter, which we attribute to weaker thermospheric inter-hemispheric circulation at aphelion compared to perihelion.

[91] 3. There appears a repeatable 20–30% density increase near aphelion at most southern latitudes.

[92] 4. The broad low in Southern Hemisphere winter densities in the upper thermosphere, which occurs around aphelion shifts progressively later with respect to the Martian seasons as the solar cycle progresses from solar max to solar min, although dust loading could still play a part in this variation.

[93] 5. There is no presently understood effect at these altitudes from the 2001 global dust storm (MY25/180°–250°). An evolving inter-hemispheric circulation during the course of the Martian year (particularly during dust storm onset and decay) may be responsible.

[94] These densities were compared to equivalent predictions for a subset of seasonal conditions from two general circulation models of the Martian atmosphere, the LMD-MGCM and MTGCM. We find that the former usually overestimates and the latter usually underestimates the densities, while both predict stronger southern winter polar warming than is observed.

[95] Despite the large inherent uncertainties, this data set of remotely sensed densities is useful in characterizing the interannual behavior of the Martian upper thermosphere/lower exosphere, and can serve as a baseline in advance of the much higher quality, species-specific in situ neutral density measurements from 120 km-350 km altitude expected from the Neutral Gas Ion Mass Spectrometer (NGIMS) instrument

aboard the Mars Atmosphere Volatile EvolutioN (MAVEN) mission (http:lasp.colorado.edu/maven), due to start taking science data in October 2014.

Appendix A: Limited Upper Thermospheric Density Probing in Strong Crustal Magnetic Field Regions

[96] Here we summarize the density probing method described by *Lillis et al*. [2008a]. In order to use measured loss cones to solve for atmospheric neutral densities, we require accurate knowledge of the total (i.e., internal plus external) magnetic field *B(x)* between the spacecraft (i.e., measurement) location and the collisional atmosphere where the electrons scatter. Since magnetic field is only directly measured at the spacecraft (B_0 in equation (1)), information for the remainder of the profile must come from elsewhere. In the work of *Lillis et al.* [2008a], to calculate this profile we used the *Cain et al.* [2003] spherical harmonic model of the internal magnetic field of Mars. This model is based upon MAG data collected at a range of altitudes between 100 km and 400 km and is typically more accurate the stronger the crustal field compared with the external field.

[97] In an effort to use the most accurate magnetic profiles, we only considered geographic regions where (1) the radial component of the model field was greater than 50 nT and therefore dominated over the external field (typically 8–15 nT on the nightside [*Ferguson et al.*, 2005]), (2) the field lines traced from spacecraft altitude down into the collisional atmosphere; i.e., the topology was open, allowing loss cones to form and (3) the measured magnetic field of the spacecraft location agreed with the *Cain et al.* [2003] model to within 5% in field strength and 10° in direction. This left us with a limited coverage of (depending on geographic bin size) 1–2% of Mars (see Figure 6) [*Lillis et al.*, 2008a].

[98] Atmospheric models such as the Mars Thermospheric Global Circulation Model (MTGCM) [e.g., *Bougher et al.*, 1990] are unconstrained by other data at the altitudes where densities affect loss cone shapes (i.e., ~170 km–230 km [*Lillis et al.*, 2008a]). Therefore, for our neutral density profile, an isothermal, 2-species (CO_2, O) atmosphere was assumed and was parameterized by a single temperature and the densities of the two species at a single height (160 km). This 3-parameter approach was the simplest representation that still captured the 2-species character of the Mars upper thermosphere and did not rely on profiles taken from any atmospheric model. However, electron loss cones are not very sensitive to changes over the expected range of neutral density profiles, shifting by < 10° for an order of magnitude increase or decrease in neutral density while the angular resolution of the ER instrument is 22.5° [*Mitchell et al.*, 2001], as can be seen in Figure 3. As a result, the 3 individual parameters could not be separately constrained and the loss cone shapes were only sensitive to the total mass density at altitudes in the range 170–210 km, with the mean altitude of greatest sensitivity at 185 km Also, these total mass densities had typical standard deviations of almost one order of magnitude, necessitating the averaging together of several hundred data points per latitude and time interval to reduce statistical errors.

[99] In addition to scientific results concerning seasonal and interannual changes in upper thermospheric densities, the main relevant result of this work was the mean loss cone-derived mass density at 185 km of 6.6 g/km^3 for these geographic locations over the 4 Martian year period from 04/1999–11/2006, which is important for the second major use of ER data covered in section 2.2.

[100] **Acknowledgments.** This work was generously funded by the NASA Mars Data Analysis Program, grants NNX07AV42G and NNX07AO84G. We would like to thank Don Woodraska for helpful information regarding the TIMED-SEE data.

References

Acuña, M. H., et al. (1992), Mars Observer Magnetic Fields Investigation, *J. Geophys. Res.*, *97*, 7799–7814, doi:10.1029/92JE00344.

Anderson, K. A., R. P. Lin, J. E. McCoy, and R. E. McGuire (1976), Measurements of lunar and planetary magnetic fields by reflection of low energy electrons, *Space Sci. Instrum.*, *1*, 439–470.

Angelats i Coll, M., F. Forget, M. A. López-Valverde, P. L. Read, and S. Lewis (2004), Upper atmosphere of Mars up to 120 km: Mars Global Surveyor data analysis with the LMD general circulation model, *J. Geophys. Res.*, *109*, E01011, doi:10.1029/2003JE002163.

Angelats i Coll, M., F. Forget, M. A. López-Valverde, and F. Gonzalez-Galindo (2005), The first Mars thermospheric general circulation model: The Martian atmosphere from the ground to 240 km, *Geophys. Res. Lett.*, *32*, L04201, doi:10.1029/2004GL021368.

Bell, J. M., S. W. Bougher, and J. R. Murphy (2007), Vertical dust mixing and the interannual variations in the Mars thermosphere, *J. Geophys. Res.*, *112*, E12002, doi:10.1029/2006JE002856.

Bertaux, J.-L., et al. (2005), Nightglow in the upper atmosphere of Mars and implications for atmospheric transport, *Science*, *307*, 566–569, doi:10.1126/science.1106957.

Bougher, S. W., R. G. Roble, E. C. Ridley, and R. E. Dickinson (1990), The Mars thermosphere: 2. General circulation with coupled dynamics and composition, *J. Geophys. Res.*, *95*, 14,811–14,827, doi:10.1029/JB095iB09p14811.

Bougher, S. W., G. Keating, R. Zurek, J. Murphy, R. Haberle, J. Hollingsworth, and R. T. Clancy (1999a), Mars Global Surveyor aerobraking: Atmospheric trends and model interpretation, *Adv. Space Res.*, *23*, 1887–1897, doi:10.1016/S0273-1177(99)00272-0.

Bougher, S. W., S. Engel, R. G. Roble, and B. Foster (1999b), Comparative terrestrial planet thermospheres: 2. Solar cycle variation of global structure and winds at equinox, *J. Geophys. Res.*, *104*, 16,591–16,611, doi:10.1029/1998JE001019.

Bougher, S. W., S. Engel, R. G. Roble, and B. Foster (2000), Comparative terrestrial planet thermospheres: 3. Solar cycle variation of global structure and winds at solstices, *J. Geophys. Res.*, *105*, 17,669–17,692, doi:10.1029/1999JE001232.

Bougher, S. W., S. Engel, D. P. Hinson, and J. R. Murphy (2004), MGS Radio Science electron density profiles: Interannual variability and implications for the neutral atmosphere, *J. Geophys. Res.*, *109*, E03010, doi:10.1029/2003JE002154.

Bougher, S. W., J. M. Bell, J. R. Murphy, P. G. Withers, and M. López-Valverde (2006), Polar warming in the Mars lower thermosphere: Seasonal variations owing to changing insolation and dust distributions, *Geophys. Res. Lett.*, *33*, L02203, doi:10.1029/2005GL024059.

Bougher, S. W., J. M. Bell, B. M. Steers, G. M. Keating, and J. R. Murphy (2007), Winter polar warming in the Mars thermosphere, in *Seventh International Conference on Mars, July 9–13, 2007, Pasadena CA* [CD-ROM], *LPI Contrib.*, 1353, Abstract 3027.

Bougher, S. W., T. M. McDunn, K. A. Zoldak, and J. M. Forbes (2009), Solar cycle variability of Mars dayside exospheric temperatures: Model evaluation of underlying thermal balances, *Geophys. Res. Lett.*, *36*, L05201, doi:10.1029/2008GL036376.

Brain, D. A., R. J. Lillis, D. L. Mitchell, J. S. Halekas, and R. P. Lin (2007), Electron pitch angle distributions as indicators of magnetic field topology near Mars, *J. Geophys. Res.*, *112*, A09201, doi:10.1029/2007JA012435.

Cain, J. C., B. B. Ferguson, and D. Mozoni (2003), An n = 90 internal potential function of the Martian crustal magnetic field, *J. Geophys. Res.*, *108*(E2), 5008, doi:10.1029/2000JE001487.

Crider, D. H., D. Vignes, A. M. Krymskii, T. K. Breus, N. F. Ness, D. L. Mitchell, J. A. Slavin, and M. Acuña (2003), A proxy for determining solar wind dynamic pressure at Mars using Mars Global Surveyor data, *J. Geophys. Res.*, *108*(A12), 1461, doi:10.1029/2003JA009875.

Ferguson, B. B., J. C. Cain, D. H. Crider, D. A. Brain, and E. M. Harnett (2005), External fields on the nightside of Mars at Mars Global Surveyor mapping altitudes, *Geophys. Res. Lett.*, *32*, L16105, doi:10.1029/2004GL021964.

Fillingim, M. O., L. M. Peticolas, R. J. Lillis, D. A. Brain, J. S. Halekas, D. Lummerzheim, and S. W. Bougher (2010), Localized ionization patches in the nighttime ionosphere of Mars and their electrodynamic consequences, *Icarus*, *206*, 112–119, doi:10.1016/j.icarus.2009.03.005.

Forbes, J. M., A. F. C. Bridger, M. E. Hagan, S. W. Bougher, J. L. Hollingsworth, G. M. Keating, and J. R. Murphy (2002), Nonmigrating tides in the thermosphere of Mars, *J. Geophys. Res.*, *107*(E11), 5113, doi:10.1029/2001JE001582.

Forbes, J. M., F. G. Lemoine, S. L. Bruinsma, M. D. Smith, and X. Zhang (2008), Solar flux variability of Mars' exosphere densities and temperatures, *Geophys. Res. Lett.*, *35*, L01201, doi:10.1029/2007GL031904.

Forget, F., F. Montmessin, J.-L. Bertaux, F. González-Galindo, S. Lebonnois, E. Quémerais, A. Reberac, E. Dimarellis, and M. A. López-Valverde (2009), Density and temperatures of the upper Martian atmosphere measured by stellar occultations with Mars Expresss SPICAM, *J. Geophys. Res.*, *114*, E01004, doi:10.1029/2008JE003086.

González-Galindo, F., M. A. López-Valverde, M. Angelats-i-Coll, and F. Forget (2005), Extension of a Martian GCM to thermospheric altitudes: UV heating and photochemical models, *J. Geophys. Res.*, *110*, E09008, doi:10.1029/2004JE002312.

González-Galindo, F., F. Forget, M. A. López-Valverde, M. Angelats i Coll, and E. Millour (2009), A ground-to-exosphere Martian general circulation model: 1. Seasonal, diurnal, and solar cycle variation of thermospheric temperatures, *J. Geophys. Res.*, *114*, E04001, doi:10.1029/2008JE003246.

Haberle, R. M., et al. (1999), General Circulation Model simulations of the Mars Pathfinder atmospheric structure investigation/meteorology data, *J. Geophys. Res.*, *104*, 8957–8974, doi:10.1029/1998JE900040.

Haberle, R. M., J. R. Murphy, and J. Schaeffer (2003), Orbital change experiments with a Mars general circulation model, *Icarus*, *161*, 66–89, doi:10.1016/S0019-1035(02)00017-9.

Joshi, M., R. Haberle, J. Hollingsworth, and D. Hinson (2000), A comparison of MGS Phase 1 aerobraking radio occultation data and the NASA Ames Mars GCM, *J. Geophys. Res.*, *105*, 17,601–17,615, doi:10.1029/1999JE001217.

Judge, D. L., H. S. Ogawa, D. R. McMullin, and P. Gangopadhyay (2000), The SoHO CELIAS/SEM data base, *Phys. Chem. Earth Part C*, *25*, 417–420, doi:10.1016/S1464-1917(00)00047-7.

Keating, G. M., et al. (1998), The structure of the upper atmosphere of Mars: In-situ accelerometer measurements from Mars Global Surveyor, *Science*, *279*, 1672–1676.

Keating, G. M., M. Theriot Jr., R. Tolson, S. Bougher, F. Forget, and J. Forbes (2003), Global measurement of the Mars upper atmosphere: In-situ accelerometer measurements from Mars Odyssey 2001 and Mars Global Surveyor, *Lunar Planet. Sci.*, *XXXVI*, Abstract 1142.

Keating, G. M., S. W. Bougher, M. E. Theriot, R. H. Tolson, R. C. Blanchard, R. W. Zurek, J. M. Forbes, and J. R. Murphy (2006), Initial Mars upper atmospheric structure results from the accelerometer science experiment aboard Mars Reconnaissance Orbiter, *Eos Trans. AGU*, *87*(52), Fall Meet. Suppl., Abstract 33A–06.

Leblanc, F., J. Y. Chaufray, J. Lilensten, O. Witasse, and J.-L. Bertaux (2006), Martian dayglow as seen by the SPICAM UV spectrograph on Mars Express, *J. Geophys. Res.*, *111*, E09S11, doi:10.1029/2005JE002664.

Lefevre, F., S. Lebonnois, F. Montmessin, and F. Forget (2004), Three-dimensional modeling of ozone on Mars, *J. Geophys. Res.*, *109*, E07004, doi:10.1029/2004JE002268.

Lillis, R. J., D. L. Mitchell, R. P. Lin, J. E. P. Connerney, and M. H. Acuña (2004), Mapping crustal magnetic fields at Mars using electron reflectometry, *Geophys. Res. Lett.*, *31*, L15702, doi:10.1029/2004GL020189.

Lillis, R. J., J. H. Engel, D. L. Mitchell, D. A. Brain, R. P. Lin, S. W. Bougher, and M. H. Acuña (2005), Probing upper thermospheric neutral densities at Mars using electron reflectometry, *Geophys. Res. Lett.*, *32*, L23204, doi:10.1029/2005GL024337.

Lillis, R. J., D. L. Mitchell, D. A. Brain, R. P. Lin, S. W. Bougher, and M. H. Acuña (2008a), Continuous monitoring of night side upper thermospheric mass densities in the Martian southern hemisphere over 4 Martian years using electron reflectometry, *Icarus*, *194*, 562–574, doi:10.1016/j.icarus.2007.09.031.

Lillis, R. J., D. L. Mitchell, R. P. Lin, and M. H. Acuña (2008b), Electron reflectometry in the Martian atmosphere, *Icarus*, *194*, 544–561, doi:10.1016/j.icarus.2007.09.030.

Lillis, R. J., D. L. Mitchell, H. V. Frey, R. P. Lin, M. H. Acuña, and S. W. Bougher (2008c), An improved crustal magnetic field map of Mars from electron reflection magnetometry: Highland volcano magmatic history and the end of the Martian dynamo, *Icarus*, *194*, 575–596, doi:10.1016/j.icarus.2007.09.032.

Lillis, R. J., M. O. Fillingim, L. M. Peticolas, D. A. Brain, R. P. Lin, and S. W. Bougher (2009), The nightside ionosphere of Mars: Modeling the effects of crustal magnetic fields and electron pitch angle distributions on electron impact ionization, *J. Geophys. Res.*, *114*, E11009, doi:10.1029/2009JE003379.

López-Valverde, M. A., D. P. Edwards, M. López-Puertas, and C. Roldán (1998), Non-local thermodynamic equilibrium in general circulation models of the Martian atmosphere: 1. Effects of the local thermodynamic equilibrium approximation on thermal cooling and solar heating, *J. Geophys. Res.*, *103*, 16,799–16,811, doi:10.1029/98JE01601.

Lundin, R., S. Barabash, A. Fedorov, M. Holmström, H. Nilsson, J.-A. Sauvaud, and M. Yamauchi (2008), Solar forcing and planetary ion escape from Mars, *Geophys. Res. Lett.*, *35*, L09203, doi:10.1029/2007GL032884.

Magalhães, J. A., J. T. Schofeld, and A. Seiff (1999), Results of the Mars Pathfinder atmospheric structure investigation, *J. Geophys. Res.*, *104*, 8943–8955, doi:10.1029/1998JE900041.

Mazarico, E., M. T. Zuber, F. G. Lemoine, and D. E. Smith (2008), Observation of atmospheric tides in the Martian exosphere using Mars Reconnaissance Orbiter radio tracking data, *Geophys. Res. Lett.*, *35*, L09202, doi:10.1029/2008GL033388.

McDunn, T., S. W. Bougher, J. Murphy, M. D. Smith, F. Forget, J.-L. Bertaux, and F. Montmessin (2010), Simulating the density and thermal structure of the middle atmosphere (~80–130 km) of Mars using the MGCM-MTGCM: A comparison with MEX-SPICAM observations, *Icarus*, *206*, 5–17, doi:10.1016/j.icarus.2009.06.034.

Mitchell, D. L., R. P. Lin, C. Mazelle, H. Rème, P. A. Cloutier, J. E. P. Connerney, M. H. Acuña, and N. F. Ness (2001), Probing Mars' crustal magnetic field and ionosphere with the MGS electron reflectometer, *J. Geophys. Res.*, *106*, 23,419–23,427, doi:10.1029/2000JE001435.

Montmessin, F., F. Forget, P. Rannou, M. Cabane, and R. M. Haberle (2004), Origin and role of water ice clouds in the Martian water cycle as inferred from a general circulation model, *J. Geophys. Res.*, *109*, E10004, doi:10.1029/2004JE002284.

Newman, C. E., S. R. Lewis, P. L. Read and F. Forget (2002), Modeling the dust cycle in a Mars general circulation model: 1. Representations of dust transport processes, *J. Geophys. Res.*, *107*(E12), 5123, doi:10.1029/2002JE001910.

Newman, C. E., S. R. Lewis, and P. L. Read (2005), The atmospheric circulation and dust activity in different orbital epochs on Mars, *Icarus*, *174*, 135–160, doi:10.1016/j.icarus.2004.10.023.

Nier, A. O., and M. B. McElroy (1977), Composition and structure of Mars' upper atmosphere: Results from the Neutral Mass Spectrometers on Viking 1 and 2, *J. Geophys. Res.*, *82*, 4341–4349, doi:10.1029/JS082i028p04341.

Parks, G. (2004), *Physics of Space Plasmas*, 125 pp., Westview, Boulder, Colo.

Paxton, L. J., and D. E. Anderson (1992), Far ultraviolet remote sensing of Venus and Mars, in *Venus and Mars: Atmospheres, Ionospheres, and Solar Wind Interactions*, *Geophys. Monogr. Ser.*, vol. 66, edited by J. G. Luhmann et al., pp. 113–189, AGU, Washington, D. C.

Seth, S. P., and V. Brahmananda Rao (2008), Evidence of baroclinic waves in the upper atmosphere of Mars using the Mars Global Surveyor accelerometer data, *J. Geophys. Res.*, *113*, A10305, doi:10.1029/2008JA013165.

Smith, D. E., et al. (2001), Mars Orbiter Laser Altimeter: Experiment summary after the first year of global mapping of Mars, *J. Geophys. Res.*, *106*, 23,689–23,722, doi:10.1029/2000JE001364.

Smith, M. D. (2004), Interannual variability in TES atmospheric observations of Mars during 1999–2003, *Icarus*, *167*, 148–165, doi:10.1016/j.icarus.2003.09.010.

Smith, M. D. (2009), THEMIS observations of Mars aerosol optical depth from 2002–2008, *Icarus*, *202*, 444–452, doi:10.1016/j.icarus.2009.03.027.

Smith, M. D., B. J. Conrath, J. C. Pearl, and P. R. Christensen (2002), Thermal emission spectrometer observations of Martian planet-encircling dust storm 2001A, *Icarus*, *157*, 259–263, doi:10.1006/icar.2001.6797.

Suarez, M. J., and L. L. Takacs (1995), Technical report series on global modeling and data assimilation, vol. 5: Documentation of the AIRES/GEOS dynamical core, version 2, *NASA Tech. Memo. 104606*, Greenbelt, Md.

Sung, K., and J. L. Fox (2001), Electron impact cross sections for use in modeling the ionospheres/thermospheres of the Earth and planets, *Eos. Trans. AGU*, *81*(48), Fall Meet. Suppl., Abstract SA52A-11.

Tolson, R. H., G. M. Keating, R. W. Zurek, S. W. Bougher, C. G. Justus, and D. C. Fritts (2007), Application of accelerometer data to atmospheric modeling during aerobraking operations, *J. Spacecr. Rockets*, *44*, 1172–1179, doi:10.2514/1.28472.

Tolson, R., E. Bemis, S. Hough, K. Zaleski, G. Keating, J. Shidner, S. Brown, A. Brickler, M. Scher, and P. Thomas (2008), Atmospheric modeling using accelerometer data during Mars Reconnaissance Orbiter

aerobraking operations, *J. Spacecr. Rockets*, *45*, 511–518, doi:10.2514/1.34301.

Tracadas, P. W., M. Zuber, D. Smith, and F. G. Lemoine (2001), Density structure of the upper thermosphere of Mars from measurements of air drag on the Mars Global Surveyor spacecraft, *J. Geophys. Res.*, *106*, 23,349–23,357, doi:10.1029/2000JE001418.

Valeille, A., V. Tenishev, S. W. Bougher, M. R. Combi, and A. F. Nagy (2009a), Three-dimensional study of Mars upper-thermosphere/ionosphere and hot oxygen corona: 1. General description and results at equinox for solar low conditions, *J. Geophys. Res.*, *114*, E11005, doi:10.1029/2009JE003388.

Valeille, A., M. R. Combi, S. W. Bougher, V. Tenishev, and A. F. Nagy (2009b), Three-dimensional study of Mars upper-thermosphere/ionosphere and hot oxygen corona: 2. Solar cycle, seasonal variations and evolution over history, *J. Geophys. Res.*, *114*, E11006, doi:10.1029/2009JE003389.

Voorhies, C. V. (2008), Thickness of the magnetic crust of Mars, *J. Geophys. Res.*, *113*, E04004, doi:10.1029/2007JE002928.

Wilson, R. J. (2002), Evidence for nonmigrating thermal tides in the Mars upper atmosphere from the Mars Global Surveyor accelerometer experiment, *Geophys. Res. Lett.*, *29*(7), 1120, doi:10.1029/2001GL013975.

Withers, P. G. (2006), MGS and Mars Odyssey accelerometer observations of the Martian upper atmosphere during aerobraking, *Geophys. Res. Lett.*, *33*, L02201, doi:10.1029/2005GL024447.

Withers, P. G., S. W. Bougher, and G. M. Keating (2003), The effects of topographically controlled thermal tides in the Martian upper atmosphere as seen by the MGS Accelerometer, *Icarus*, *164*, 14–32, doi:10.1016/S0019-1035(03)00135-0.

Withers, P., M. Mendillo, H. Rishbeth, D. P. Hinson, and J. Arkani-Hamed (2005), Ionospheric characteristics above Martian crustal magnetic anomalies, *Geophys. Res. Lett.*, *32*, L16204, doi:10.1029/2005GL023483.

Woods, T. N., and F. G. Eparvier (2006), Solar ultraviolet variability during the TIMED mission, *Adv. Space Res.*, *37*, 219–224, doi:10.1016/j.asr.2004.10.006.

S. W. Bougher, Department of Atmospheric, Oceanic and Space Sciences, University of Michigan, 2455 Hayward St., Ann Arbor, MI 48109-2143, USA.

P. C. Chamberlin and M. D. Smith, NASA Goddard Space Flight Center, Greenbelt, MD 20771, USA.

F. Forget and F. González-Galindo, Laboratoire de Météorologie Dynamique, Institute Pierre Simon Laplace, F-75005 Paris, France.

R. J. Lillis, Space Sciences Laboratory, University of California, 7 Gauss Way, Berkeley, CA 94720, USA.